ELSEVIER

PROGRESS IN NUCLEAR MAGNETIC RESONANCE SPECTROSCOPY

Progress in Nuclear Magnetic Resonance Spectroscopy 40 (2002) 275–306

www.elsevier.com/locate/pnmrs

Small animal neuroimaging using magnetic resonance microscopy

E.T. Ahrens[a,b], P.T. Narasimhan[b], T. Nakada[c], R.E. Jacobs[b,c,*]

[a]*Department of Biological Sciences, Carnegie Mellon University, Pittsburgh, PA 15213, USA*
[b]*Biological Imaging Center, Beckman Institute, California Institute of Technology, Pasadena, CA 91125, USA*
[c]*Department of Integrated Neuroscience, Brain Research Institute, University of Niigata, Niigata 951-8585, Japan*

Accepted 20 January 2002

Contents

* Corresponding author. Address: Biological Imaging Center, Beckman Institute, California Institute of Technology, Pasadena, CA 91125, USA. Tel.: +1-626-449-5163; fax: +1-626-395-2849.
E-mail address: rjacobs@caltech.edu (R.E. Jacobs).

PII: S0079-6565(02)00003-1

Nomenclature

BOLD blood-oxygen-level-dependent
CHESS chemical shift selective
CPMG Carr–Purcell–Meiboom–Gill
CSI chemical shift imaging
DQF double quantum filter
EPI echo planar imaging
FLASE fast-large-angle-spin-echo
FLASH fast-low-angle-shot
FSE fast spin-echo
GE gradient-echo
GESEPI gradient-echo slice excitation profile imaging
HSel-MQC hard pi pulse Sel-MQC
i-MQC intermolecular multiple quantum coherence
i-DQC intermolecular double quantum coherence
ISIS image selected in vivo spectroscopy
i-ZQC intermolecular zero quantum coherence
PGSE pulsed-gradient spin-echo
PGSE-MASSEY pulse gradient spin-echo modulus addition using spatially separated echo spectroscopy
PGSTE pulse gradient stimulated echo
PRESS point resolved spectroscopy
RARE rapid acquisition with relaxation enhancement
SE spin-echo
SEE-SelMQC spin-echo enhanced SelMQC
Sel-MQC selective homonuclear multiple quantum coherence
SSel-MQC selective pi pulse Sel-MQC
STEAM stimulated echo acquisition mode

1. Introduction

Magnetic resonance imaging (MRI) provides three-dimensional (3D) non-invasive views into optically opaque tissues with exquisite sensitivity to the local physical and chemical environments. MR images provide knowledge about the internal structure and function of intact living systems. The wide range of mechanisms giving rise to intrinsic MRI contrast furnishes images with dramatic differences between different tissue types. High resolution MRI, magnetic resonance microscopy (μMRI), is an emerging technique capable of imaging biological subjects in vitro and in vivo at near-cellular resolution. Tissue morphological changes, progression of disease states, and biochemical changes may all be visualized with μMRI. In the research setting, small animal models of development and disease are often the subject of study. The capabilities of μMRI make it an ideal complement to long standing optical imaging methods used in studying these systems. Using μMRI methods, it is possible to routinely produce 3D images with an isotropic resolution of less than 50 μm. Future advancements in μMRI imaging technologies that focus on the central nervous system (CNS) will be truly interdisciplinary in nature. These advances will benefit basic biological and biomedical science and may stimulate new directions and applications in clinical diagnostic imaging.

The challenges associated with in vivo μMRI are threefold: achieving adequate signal in the intrinsically noisy MR experiment, obtaining sufficient contrast to distinguish important features in the specimen, and minimizing the effects of subject motion. First, one must achieve an adequate image signal-to-noise ratio (SNR) from the microscopic image volume

elements (voxels). For example, the water proton concentration in tissue is essentially that of liquid water (110 M). A volume element 1 mm on each side will contain 1 μl of water or $\sim 10^{-4}$ mol of proton spins, while a voxel 10 μm on each side will contain $\sim 10^{-10}$ mol of proton spins. With such a small number of spins, the SNR determines the practical limit to image resolution in μMRI. Ways of optimizing SNR in the μMRI experiment include working at very high magnetic field strengths, customizing radio-frequency (RF) detection hardware for the specific specimens of interest, and tailoring the imaging pulse sequences. Contrast allows one to delineate anatomical features of interest in the MR image. Thus, it is crucial to have a sufficiently large image contrast-to-noise ratio (CNR), defined as the difference between the SNR of distinct tissue types (e.g. gray and white matter). Contrast originates from differences in physical properties among the tissues, such as T_1, T_2, water diffusivity, and spin density. There are many other contrast mechanisms, as well as experimental ways of altering the contrast in the MR image. These include employing particular pulse sequences and the addition of exogenous agents. Because the subjects under investigation are living and breathing creatures, it is essential to immobilize the subject in a humane fashion in order to minimize image artifacts. This must be achieved while maintaining the physiological stability of the subject for extended imaging sessions.

In this review, we will consider applications of μMRI in small animal model systems. Experimental hardware is often a limiting factor in these studies and serves as a convenient means to limit the scope of this review. For the most part, we will limit consideration to work carried out at high magnetic field strengths (>4 T) with small bore sized magnets (<20 cm). Moreover, because brain imaging tests the technical, theoretical, and interpretive aspects of MRI, we will emphasize efforts involving studies of the CNS. Our aim is to describe several promising areas that are pushing the state-of-the-art of μMRI. In Section 2.1, we briefly discuss basic concepts of MRI; in Section 2.2, we introduce issues pertaining to the difficulty of obtaining microscopic resolution MR images; the rest of Section 2 covers different ways of performing the MRI experiment that provide particular types of contrast or information about tissues of interest; in Section 3, we review applications of small animal μMRI in several biological realms. The goal of this review is not to provide an exhaustive survey of all results and methodologies in small animal μMRI, but rather to make the reader aware of the types of techniques employed and provide a flavor for the types of studies that are feasible with current high field μMRI methods.

2. Background

2.1. MRI basics

The physical basis of MRI has been reviewed by numerous authors (for example, see Refs. [1–3]). Here, we briefly summarize key concepts. In order to obtain information about the spatial location of the spins, MRI makes use of magnetic field gradients. When a uniform sample containing protons (or other NMR active nuclei) is placed in a linear magnetic field gradient $G_x = \mathrm{d}B_z/\mathrm{d}x$, applied along $\hat{x}$, the result will be a distribution of Larmor frequencies. By superimposing this small magnetic field gradient into a large static field (B_0) along $\hat{z}$, the Larmor frequency distribution will take the form

$$\omega(x) = \omega_0 + \gamma x G_x, \tag{1}$$

where γ is the gyromagnetic ratio, and $\omega_0 = \gamma B_0$. In this way, spatial information is mapped into the frequency domain. This procedure is referred to as *frequency encoding*.

An ensemble of spins processing in a magnetic field gradient tends to dephase. For a phase-coherent spin population at time $t = 0$, the presence of a constant gradient G_y imparts a phase ϕ_y during a period of time t_y given by

$$\phi_y = \gamma y G_y t_y. \tag{2}$$

By using gradients along different directions, one can label the positions of the spins by their ϕ values. This forms the basis of *phase encoding*, which is another way to encode spatial information. In the case of a time-varying gradient, we have the relation:

$$\phi_y = \gamma \int y G_y(t) \mathrm{d}t. \tag{3}$$

One can excite spins within a slice of a specimen of

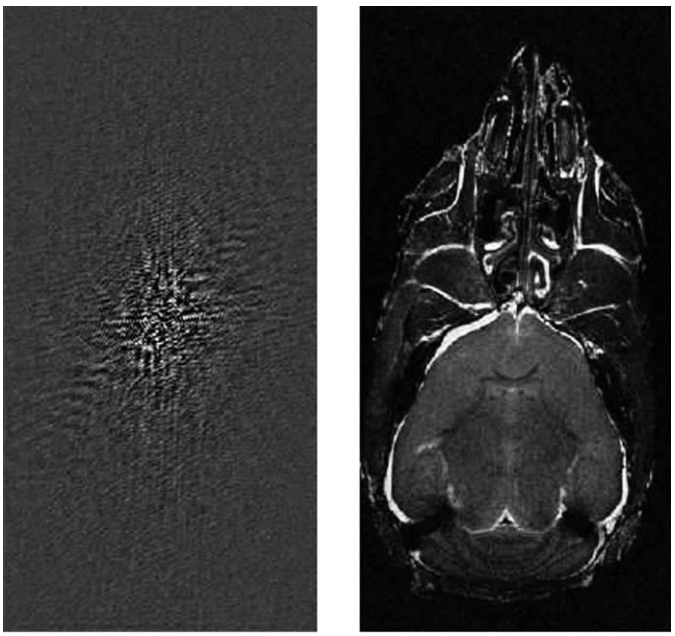

Fig. 1. MRI data are originally collected in k-space then Fourier transformed to obtain information that is readily interpretable by the human eye. The left panel shows k-space data with the origin at the center of the rectangle. Data values are mapped onto a gray scale such that the maximum positive value is white, zero is neutral gray, and largest negative value is black. The right panel shows the result of 2D Fourier transformation of data in the left panel revealing a horizontal slice through a live mouse head.

specified thickness and orientation by the simultaneous application of a RF pulse and a magnetic field gradient. The shape of the RF pulse is tailored to excite spins within a chosen bandwidth, $\Delta\omega$ [1]. The value and duration of slice selecting magnetic field gradient G_z is set to excite spins only within this bandwidth; this defines a slice in the spatial domain of width (Δz) given by

$$\Delta z = \frac{\Delta\omega}{\gamma G_z}. \tag{4}$$

By using a combination of slice selection, phase encoding, and frequency encoding, one can construct imaging pulse sequences. Two-dimensional (2D) sequences often utilize these three ingredients, where each function is assigned to an orthogonal direction, such as in Eqs. (1), (3) and (4). A 3D image can be obtained using a combination of two phase and one frequency encoding directions. Neglecting relaxation effects, the signal (S) obtained at the end of the phase and frequency encoding periods in which a 90° pulse is used for excitation is

$$S(\vec{k}) \propto \int\int\int \rho(\vec{r})\exp(\mathrm{i}\vec{k}\cdot\vec{r})\mathrm{d}^3\vec{r}, \tag{5}$$

where $\rho(\vec{r})$ is the spin density distribution, and $\vec{k}$ is defined by

$$\vec{k} = \gamma\sum_i G_i t_i \hat{i}, \tag{6}$$

where $i = x, y, z$ and t_i is the gradient duration. Eq. (5) has the form of a Fourier transform (FT) with $\vec{k}$ and $\vec{r}$ as conjugate variables, hence

$$\rho(\vec{r}) \propto \int\int\int S(\vec{k})\exp(-\mathrm{i}\vec{k}\cdot\vec{r})\mathrm{d}^3k. \tag{7}$$

Thus, the FT connects the raw MRI data acquired in 'k-space' to a spin-density map in the spatial domain. Fig. 1(a) and (b) shows examples of a k-space map and the resulting image after Fourier transformation, respectively. The central portions of the k-space map

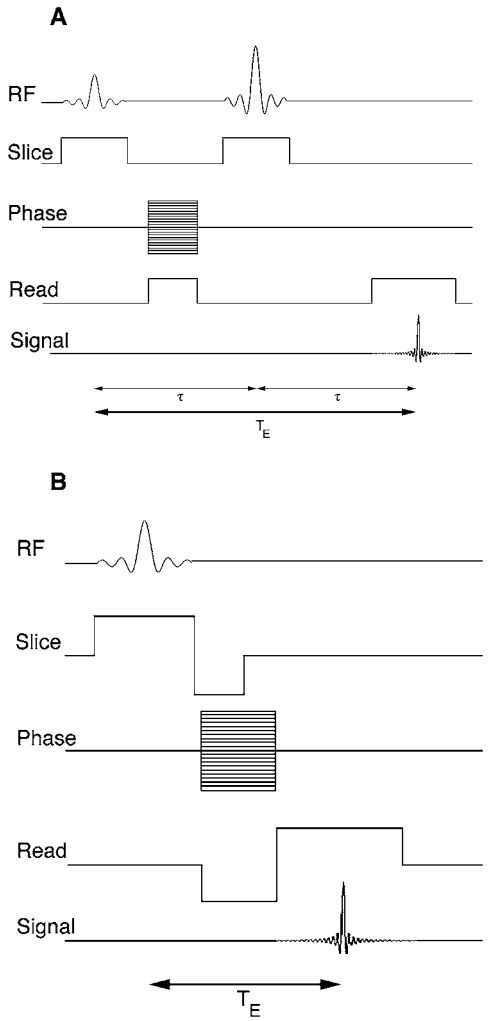

Fig. 2. (A) Typical 2D SE sequence. The 90° (lower amplitude) and 180° RF pulse are slice selective, a different value of the 'phase' gradient is employed for each line in k-space which is acquired as the 'echo' under the 'read' gradient. In this fashion, the row-location of a data point in Fig. 1 is determined by the value of its phase gradient and its column is determined by where it occurs under the read gradient. (B) Typical 2D GE sequence. In this protocol, the initial negative valued portion of the read gradient served to reverse the phase of the spins so that they are refocused by the positive valued portion of the read gradient.

(Fig. 1(a)) have the highest signal intensity and provide the dominant contribution to image contrast. The edges of the k-space map correspond to higher spatial frequencies and contribute boundaries and image details [4,5].

Examples of basic 2D imaging schemes are shown in Fig. 2(a) and (b) for spin-echo (SE) and gradient-echo (GE) sequences, respectively. In both sequences, an echo is acquired in the presence of the frequency-encoding gradient (G_x) for each value of the phase-encoding gradient G_y, and the slice-plane is perpendicular to the z-direction. The G_y-values are usually incremented in equally spaced steps that take both positive and negative values; the echo is 'readout' for each step as G_x is applied. In this fashion k-space is filled line-by-line. The 2D SE sequence in Fig. 2(a) is known as the 2D-FT spin-warp imaging sequence [6]. Fig. 2(b) shows the corresponding GE version for 2D imaging. Instead of using a 180° RF refocusing pulse, the GE sequence reverses the read-out gradient in order to refocus spins and obtain the echo.

The development of methods that rapidly acquire k-space data has been extremely important to the advancement of MRI. In the imaging schemes shown in Fig. 2(a) and (b), a single line of k-space is acquired for each RF excitation; raster scanning in this fashion is an inherently slow process. Other schemes, such as echo planar imaging (EPI) [7], allow one to obtain more than one or several lines of k-space or even the entire k-space map in a single RF excitation. Another example is the GE fast-low-angle-shot (FLASH) technique [8] that employs a small flip-angle for the RF excitation pulse. The small flip-angle permits rapid sequence repetition. Using EPI or FLASH, it is possible to obtain an entire image in less than a second. Such rapid imaging helps in providing immunity to motion artifacts. A review of the current state of EPI methods is described by Schmitt et al. [9].

Because of the FT relationship between k-space data points and image data points, even one corrupted data point in the k-space can affect the quality of the image. Subject movement during data acquisition can thus lead to artifacts in the image. In the context of brain imaging, two factors that cause such artifacts are physical motion and fluid motion. Flow of blood and cerebrospinal fluid (CSF) belong to the latter category. In μMRI of the brain, physical restraints to minimize head movements are recommended. Special MR techniques to compensate for motion through corrective algorithms may help further; of these, the 'navigator echo' technique makes use of additional, 'navigator,' echoes interleaved into the imaging

sequence. This method uses post-processing of the navigator echo data with the help of algorithms for adaptive correction of the effects of object motion to suppress artifacts in the final image [10].

The image intensity of tissues is determined by a number of factors. The physical properties of a specific tissue, such as spin density, T_1, T_2, T_2^*, and water diffusivity determine the amount of available signal. The CNR, or the difference between the SNR between distinct tissue types (e.g. white and gray matter), is controlled by judicious choice of data acquisition parameters in a SE or GE sequence and/or the addition of 'preparation modules' consisting of RF pulses and magnetic field gradients. The role of T_R, T_E, gradient strength, and sampling time on SNR and CNR in SE and GE imaging schemes has been reviewed by a number of authors [11–14].

In the high magnetic field strengths utilized by the MR microscopist, neural tissue contrast resulting from T_1 and T_2 mechanisms is substantially altered compared to what is observed at lower (clinical) field strengths. This is because T_1- and T_2-values in the brain are magnetic field dependent. In the case of gray and white matter, there is substantial loss of intrinsic contrast between these tissues due to a 'convergence' of their relaxation times as the magnetic field strength is increased. One way to recover from the loss of intrinsic contrast at high field strengths is via exogenous contrast agents.

Broadly, there are two classes of contrast agents (T_1 and T_2); these are distinguished by the relaxation time they predominately modulate. T_1-type agents typically consist of a lanthanide metal ion, usually Gd^{3+}, that is chelated to a low molecular weight complex to render it non-toxic. Water molecules in proximity to, and exchanging with, the paramagnetic-complex experience a reduction in T_1; consequently, contrast enhancement can result from differences in agent concentration. 'Conventional' T_1 contrast agents, such as gadolinium chelated by diethylenetriamine-pentaacetic acid (Gd-DTPA), are routinely used to enhance lesions or fluid filled compartments [15]. Contrast agent tissue concentrations in excess of 50 μM are normally required to obtain satisfactory contrast enhancement in MR images [16].

Commonly used T_2-type agents are particulates, of order of 10–100 nm in diameter, composed of magnetite ($FeO{\cdot}Fe_2O_3$) crystallites that are encapsulated in dextran [17]. These nano-particles exhibit properties of superparamagnetism [18] and are effective in causing local perturbations in the magnetic field homogeneity. This results in a loss of phase coherence among nearby nuclei and reduces T_2; thus, a reduction in image intensity occurs near the particles in T_2- or T_2^*-weighted images. The concentration of particulates needed to provide meaningful image contrast is significantly less than that with T_1-type agents.

Conventional T_1 and T_2 agents provide anatomical information, have a non-selective distribution, and are physiologically inert. However, recently there have been efforts to design 'smart' contrast agents that are intended to highlight distributions of cell surface receptors [19–21], gene expression [22], and cell function [23]. Recent advances in this area are reviewed elsewhere [24–27].

2.2. The μMRI challenge

The goal is to obtain 3D MR images of live animals at near-cellular resolutions in order to characterize the functional and anatomical consequences of many biological phenomena, including disease progression, developmental processes, and phenotypic changes in genetically manipulated animals. Given the physical and temporal constraints inherent in working with live animals, single cell resolution is currently not feasible. Nevertheless, voxel sizes of tens-of-microns obtained using μMRI offer substantially more information than voxel sizes of millimeters typically employed in clinical MRI. This reduction in voxel size in μMRI translates into a large reduction in the number of spins per voxel available for imaging. Assuming a homogenous sample, the ratio of spins in a cubic voxel of the size of 1 mm to one of 10 μm is 10^6:1, resulting in a proportional reduction in the available MR signal. The principal challenge in μMRI is to obtain sufficient SNR to provide a detailed image in a reasonable amount of time.

In addition to voxel volume, other factors affecting SNR are described in the early NMR literature [28–30]. In the context of biological MRI, it was recognized [31–33] that noise could arise not only from the receiver coil, but also from thermal Johnson noise in the sample. Sample noise is the dominant statistical noise source in clinical MRI. At high magnetic field strengths, and for the small sample sizes typically

used in μMRI, one is often in a regime where the dominant noise contribution comes from thermal noise in the receiver coil [34]. This has led to innovative efforts to optimize hardware design in the areas of micro-coils [35,36], novel probe designs [37,38], thermal cooling of the coil and preamplifier [39–42], as well as using extremely high Q coils made from cuprate high temperature superconductors [43–45].

SNR and imaging time are intimately related. One of the earliest analyses of this relationship was due to Brunner and Ernst [46] who compared different imaging techniques. These authors concluded prophetically that 'sensitivity will remain one of the insurmountable limitations of NMR techniques for biological imaging.' An approximate relationship between imaging time t_i and other key parameters in an MRI experiment was derived by Mansfield and Morris [1] and is given by

$$t_i \propto (\mathrm{SNR})^2 r^2 \left(\frac{T_1}{T_2^*}\right) \frac{1}{f^{7/2}} \left(\frac{1}{\Delta x}\right)^6, \tag{8}$$

where r is the radius of a solenoidal receiver coil, T_1 and T_2^* are the longitudinal and inhomogeneously broadened effective transverse relaxation times, respectively, f is the spectrometer frequency, and Δx is the length of a side of a cubic voxel. Note the dependence of t_i on the sixth power of the inverse voxel size. A reduction in Δx by one-half increases t_i by a factor of 64 (at a given SNR). Thus, it is clear that increased resolution comes at a high cost in terms of imaging time. When working with live animals one is often limited by the amount of time that one can safely anesthetize the subject; this in turn limits t_i. In order to acquire the data without sacrificing SNR, μMRI experiments are typically performed at high f, small r, and utilizing optimized RF hardware designs.

One of the drawbacks to working at high f is the increase in the ratio of T_1/T_2 as the magnetic field strength is increased [47]. Ahrens and Dubowitz [48] have investigated the field dependence of a related ratio, T_1/T_2, in cortical gray matter. In the human brain $T_1/T_2 = 9$ at 1.5 T [49]. By comparison, in the live mouse brain at 11.7 T, $T_1/T_2 = 60.5$, which is exceedingly large [48]. Because the imaging time increases monotonically with the parameter T_1/T_2, this observation highlights one of the fundamental difficulties associated with the implementation of rapid-imaging methods at extremely high magnetic field strengths. Another interesting complication associated with performing μMRI at high magnetic field strengths is the existence of magnetic susceptibility artifacts, and these issues are discussed below.

2.3. Magnetic susceptibility effects in high field imaging

Living samples are inhomogeneous. They possess gaseous portions (sinuses), 'gelatinous' portions (tissue), liquid portions (CSF), and solid portions (bones). Moreover, each of these gross divisions can be extensively subdivided into finer volumes based on, for example local physiological properties, the presence or absence of flow, local tissue symmetries, cell density, and chemical content. The goal of the μMR imaging experiment is to obtain an image whose features reflect important and/or interesting characteristics of the subject. The same data acquisition techniques (i.e. SE, GE, inversion-recovery, magnetization-transfer, etc.) employed in 'conventional' MRI can be used in μMRI. However, one problem encountered at low fields, but significantly more troublesome at high magnetic fields, is the deleterious effects of differences in magnetic susceptibility (χ) of different tissues across the sample.

It is well recognized that χ differences within and around an object can lead to artifacts in MR images [3,47]. For example, this can lead to unwanted signal loss in brain images in proximity to the inferior frontal lobes where marked χ differences exist across the air–tissue interface. Resolution in images obtained with GE can be seriously degraded due to the χ effect even though one would expect an improvement on account of the increased SNR with larger B_0 [2,3,50–52]. The χ effect can also be useful in providing contrast, for example, in a T_2^*-weighted fMRI experiment. Furthermore, the gradients induced by χ variations can affect quantitative diffusion imaging experiments [53] and fat suppression schemes [54]. The nature of the χ effect on images depends on the pulse sequence employed for data acquisition (e.g. GE or SE), as well as on the image processing used to construct the image, such as FT or projection reconstruction

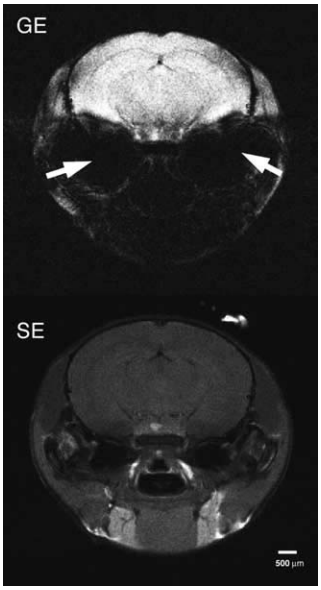

Fig. 3. GE and SE images of a live mouse recorded using an 11.7 T Bruker Avance DRX system. The top panel shows a slice acquired using a 2D GE multi-slice protocol. The bottom panel shows the same slice acquired with a 2D SE protocol. Arrows note major susceptibility artifacts in the GE image that obscure large portions of the amygdala, lateral hypothalamas, and baso-lateral cortical structures. The SE data were collected immediately following the GE data acquisition. The 2D GE experiment used a 30° excitation pulse and one scan, while SE used 90° excitation pulse and six scans (averaged). In both cases $T_R = 700$ ms, $T_E = 10$ ms, data matrix size is 256×256, field of view $= 2 \times 2$ cm^2, slice thickness $=$ 1 mm. Scale bar $= 500$; μm.

[47]. Fig. 3 shows a comparison of GE and SE images of an in vivo mouse brain acquired with comparable parameters.

Extensive studies have been made using simple geometric shaped phantoms and numerical analyses to obtain insight into χ artifacts [55–57]. Such studies have in turn helped in understanding the details of the local magnetic field distributions that cause image artifacts [58]. Largely due to the interest in fMRI, a number of studies have been made in recent years to model T_2^* contrast in terms of blood susceptibility changes, blood flow, blood volume, and other relevant parameters. Typically, such studies [59–61] model the neural vasculature as paramagnetic cylinders and vary their orientation in the magnetic field to calculate the signal contribution from diffusion in the presence of local gradients that depend on χ and B_0. In the following, we briefly examine the various methods that have been proposed for eliminating or compensating for χ-induced effects in imaging. We shall consider two types of pulse sequences, namely, GE and SE with emphasis on high field imaging, and FT image reconstruction is assumed.

2.3.1. Gradient-echo methods

Frahm et al. [50] have highlighted the role played by the slice selection gradient in 2D FLASH imaging and have proposed a slice selection gradient compensation method. In this method, the χ-induced magnetic field gradient is compensated by choosing an appropriate value of the slice selection refocusing gradient. This provides a measure of control over intravoxel dephasing due to χ-generated gradients. The method achieves compensation for only a particular local field gradient value and signals from homogenous areas and areas having different local field gradients are reduced. Further, incomplete slice refocusing can result in a shift in the mean frequency of the spin packet distribution [62]. However, both the voxel dephasing and frequency shift effects can be exploited in fMRI studies [63]. The method of Frahm et al. has been adapted [64] to multi-GE acquisitions of fMRI data obtained near the olfactory cavity where the χ difference at the air–tissue interface causes signal loss. Note that in Fig. 3, the bottom portion of the brain near cavities is most severely distorted in the GE images as compared with the SE images.

In studies of brain-iron concentrations, Ordidge et al. [65] adapted the slice selection gradient refocusing technique to correct for global field inhomogeneity contributions (T_2') to T_2^*, where $1/T_2^* = 1/T_2 + 1/T_2'$. The goal of these studies was to investigate a possible correlation between Parkinson's disease and brain-iron levels. T_2^* values were obtained using multiple gradient-echoes with different slice-select refocusing gradients, while T_2 values were obtained with spin-echoes. T_2' values were then calculated and related to the concentration of iron contained in tissue.

A technique related to Frahm's method for removing local field gradient artifacts is termed gradient-echo slice excitation profile imaging (GESEPI) [66]. By superimposing an incremental gradient offset on the slice refocusing gradient, k-space is sampled over the full range of spatial frequencies of the excitation

profile. Artifacts produced by low order field gradients in the sample are separated and removed from the high order ones responsible for T_2^* contrast by an additional Fourier transformation. Rat brain micro-imaging carried out at 9.4 T by the GESEPI method yielded images that were superior to the conventional GE method. Recently, good T_2^*-weighted images of the mouse brain with minimal χ artifacts have been obtained at 14 T by the GESEPI technique [67].

Excitation with a tailored RF pulse in GE imaging has been proposed to reduce χ effects [68]. This method utilizes an RF pulse with a quadratic phase distribution along the slice direction; however, this method suffers from reduced SNR. Tailored RF pulses based on the Shinnar-LeRoux algorithm can be employed to compensate for linear or quadratic variations along the slice thickness direction [69]. In principle, the method can be extended to the slice plane as a whole. χ-Affected signals can also be analyzed using a spectral decomposition technique [70]. In this approach, a GE imaging pulse sequence is used in which the spectroscopic information is encoded as a third dimension by incrementing the echo-time. Using post-processing, one can correct for artifacts due to χ-induced field inhomogeneity and chemical shift artifacts [71]; this procedure permits correction of χ and chemical shift artifacts after data collection independent of each other and does not require that the inhomogeneity gradient be constant or vary with position. The advantage of acquiring GE images in a higher-dimensional space and projecting them to a lower-dimensional space has been explored [72,73]. Although time consuming, 3D GE data acquired in the presence of field inhomogeneity can be processed to yield artifact-free 2D images; high quality images can be generated if phase-encoding is employed in all the three spatial dimensions [73,74].

2.3.2. Spin-echo methods

χ-variations across a subject translate into a position-dependent static field inhomogeneity, $\Delta B_0(r)$. These give rise to a frequency offset $\gamma\Delta B_0(r)$, that is, in addition to that from the read gradient in a 2D phase-frequency based imaging scheme. The image voxel dimension along the read direction is thus altered. Because the ratio of $\gamma\Delta B_0(r)$ to the read gradient, G_R, determines the size of this effect, it is advantageous to image with a high value of G_R to avoid voxel distortion. Rofe et al. [75] have experimentally demonstrated the advantage of using large gradients in μMRI for avoiding χ-induced distortion; pulse sequences utilizing 2D (i.e. slice-selective) phase-frequency and phase–phase encoding were studied. These studies used the Carr–Purcell–Meiboom–Gill (CPMG) [76] multi-pulse sequence. It was shown that phase-frequency encoding avoids χ distortion by the use of large gradients (~6 T/m); in addition, SNR can be improved by echo co-addition. Furthermore, the use of phase–phase encoding can achieve the optimal T_2-resolution limit with suppression of both χ and diffusion effects [75].

Phase evolutions accumulated by off-resonant spins are refocused in the SE sequence at the center of the echo. By sampling the signal at the exact center of the echoes in a CPMG-type sequence, it is possible to minimize field inhomogeneity and chemical shift artifacts. This idea has been incorporated by Sharp et al. [77] in their line-narrowed 2D-FT imaging method. These authors employed a train of 180° pulses and sampled the spatially encoded echoes only at their peaks. A reduction in the diffusion attenuation of the signal also results with this imaging method. Micro-MR images of single neurons from the abdominal ganglia of adult sea hares (*Aplysia californica*) have been obtained at 500 MHz by the line-narrowed 2D-FT sequence [78]. These images show clear nuclear and cytoplasmic differentiation.

There are other approaches that can be used to suppress χ inhomogeneity effects. Several studies have drawn on single-point imaging techniques that were developed originally for imaging solids [79–82]. Fast spin-echo (FSE) sequences like RARE [83–85] and its variants use RF refocused echoes, and consequently the problems associated with χ should be minimal at high fields. Furthermore, as a result of using consecutive RF pulses for refocusing, diffusion losses are minimized [86]. Other FSE sequences suitable for high field μMRI have been described by Zhou et al. [87] who have obtained good images of the rat brain at 7.1 T. Ma et al. [88] have outlined a sequence that they refer to as fast-large-angle-spin-echo (FLASE) for obtaining high quality micro-images free from intravoxel phase dispersion and χ-induced background gradients. They have provided impressive

examples of the performance of their sequence in the case of trabecular bone at 1.5 T. An evaluation of the performance of FLASE at higher fields has not been made.

The χ-induced gradient can also be used to improve image resolution. These local gradients that attenuate the signal due to diffusion may vary spatially, and at certain locations within the subject the applied read gradient may oppose the χ-generated gradient to the extent of canceling it out. Very small particles or objects with dimensions smaller than the magnetic field gradient-prescribed resolution may thus become visible in μMRI [74].

2.4. Diffusion and perfusion imaging

Some of the earliest investigations into the nuclear magnetic resonance phenomena in 1950s demonstrated that NMR could be used to measure molecular diffusion rates [86]. The generation of quantitative diffusion maps with MRI has attracted great interest [89]. In both NMR and MRI, the basic principle behind the measurement is the same—the magnetic resonance signal is sensitized to diffusion by the addition of magnetic gradient pulses that are incorporated into the pulse sequence [90]. If the nuclei are immobile, the net effect of these applied pulses on the MR signal is zero. Alternatively, any molecular motion during and between the gradient pulses causes an attenuation of the signal. In the original pulsed-gradient spin-echo (PGSE) method [90], rectangular gradient pulses of width δ and separation Δ are used to obtain the signal intensity (I) with and without (I_0) gradient pulses. The ratio of these intensities is related to the gradient strength G as

$$\ln(I/I_0) = -\gamma^2 G^2 D \delta^2 (\Delta - \delta/3). \tag{9}$$

By measuring the signal ratio as a function of G, the diffusion coefficient can be calculated. The quantity $\gamma^2 G^2 \delta^2 (\Delta - \delta/3)$ is usually denoted as the 'b-factor,' and one can write

$$\ln(I/I_0) = -bD. \tag{10}$$

The expression for the b-factor becomes more complicated in the presence of imaging gradients and non-rectangular diffusion gradients [89,91–93]; these add more complexity by introducing so-called 'cross terms' (G_i G_j terms) in addition to 'self-terms' (G_i^2 terms [94]). In isotropic media (e.g. fluids and gray matter), diffusion gradients applied along a single direction (of various strengths) can be used to acquire diffusion weighted images (DWIs). After calculating b for each DWI [89,93], the diffusion coefficient can be evaluated on a pixel-by-pixel basis to provide a map of the apparent diffusion coefficient (ADC) in the specimen.

Water diffusion in tissue is considered *restricted* [95] due to the influence of the packing and orientation of cells, and extra- and intracellular components; these impede the free self-diffusion of water. Whether or not the effects of restricted diffusion can be observed experimentally depends on the time scale of the experiment. For very short measurement times (Δ), a diffusing molecule undergoes a small net displacement and has a small probability of encountering a restrictive boundary. The molecule would appear to be freely diffusing. At longer Δ values, the probability of encountering an obstacle increases, and manifestations of restricted diffusion may be experimentally observable.

Diffusion in white matter fibers is restricted and *anisotropic* as a consequence of the orientation of the axonal fibers [96]. Diffusion anisotropy means that different diffusion rates are observed along different spatial directions. As a result, the intensity of a given voxel will vary for gradient pulses of comparable strength that are applied along different orientations. Mathematically, diffusion anisotropy can be modeled as a symmetric 3×3 tensor with six independent values corresponding to diagonal and off-diagonal elements or directions. Measurement of the effective diffusion tensor in each voxel is the basis of the method called diffusion tensor imaging (DTI) [97]. Generalizing Eqs. (9) and (10) to a tensor formalism yields

$$\ln\left(\frac{I}{I_0}\right) = -\gamma^2 \delta^2 \Delta \sum_{i,j} G_i D_{ij} G_j = -b_{ij} D_{ij}, \tag{11}$$

where $i = (x, y, z)$ and D_{ij} and b_{ij} are elements of the apparent diffusion tensor and b-matrix, respectively. The b-matrix can be calculated analytically [98] or numerically. In isotropic media $D_{xx} = D_{yy} = D_{zz}$, and the off-diagonal elements are zero.

DTI is effective in elucidating the location and directionality of white matter fiber-pathways in the

brain [99–103]. Pathways are identified on the basis of their diffusion anisotropy; other CNS tissues (e.g. gray matter, CSF, etc.) exhibit essentially isotropic diffusion. The principal axes (eigenvectors) of the *D*-tensor can be obtained by diagonalization and the principal diffusivities (eigenvalues) can be determined along these axes. In the eigenspace of each voxel containing white matter, the fiber direction is the direction of the largest eigenvalue. One of the attractive attributes of DTI is that the measurement of these eigenstates is independent of the orientation of the specimen within the magnet. Numerous scalar metrics of diffusion anisotropy have been devised that are rotationally invariant and based on the D_{ij} values or the principal diffusivities [99,100,104,105]. Another useful rotationally invariant contraction of the apparent *D*-tensor is its trace, which is the directionally averaged diffusivity. The trace of the apparent *D*-tensor provides a useful early diagnostic of cerebral ischemia [106]. Pulse sequences have been designed to obtain the trace of the apparent *D*-tensor within a single scan [107,108].

The brain and spinal cord of small animals serve as excellent subjects for investigation by DTI. However, DTI is a time-intensive imaging technique because at least seven DWIs must be obtained to fit the tensor [109,110]. Moreover, there are a number of factors that compromise the accuracy of the tensor map. Included among them are motion, SNR limitations, eddy currents, number of *b*-values (also, their pattern and magnitudes), and echo timing [110–116]. DTI has been implemented in a variety of ways; recently, these have included rapid 3D SE imaging [117,118] and echo-shifted GE imaging [119].

Perfusion refers to the amount of blood delivered to a particular volume of tissue in a given amount of time. This blood flow at the capillary level is intimately related to tissue oxygenation and the delivery of nutrients. One principal concern in measuring perfusion with MRI is differentiating it from bulk blood flow in major veins and arteries. The two main MRI methods of measuring perfusion are bolus tracking of intravascular contrast agents and arterial spin labeling [120–127]. The bolus tracking method relies on the fact that high local concentrations of a paramagnetic contrast agent (such as happens during the first pass of a bolus injection) produces a transient intensity difference between the capillaries containing the agent and the surrounding tissue. In the arterial spin labeling method, the water proton spins in a slice just upstream from the tissue of interest are tagged (typically inverted). Rapid imaging of a slice plane within the brain allows monitoring of the time course of the magnetization state of the inflowing blood. There are a large number of specific implementations of these general methods [128–134]. Modeling of the time dependence of MR signal change provides at least relative values of the desired hemodynamic information (e.g. mean transit time, CBV, and CBF) in living systems [127,135–138].

2.5. Functional neuroimaging

A key area where small animal μMRI has led to substantial advances in our understanding of the brain is the area of functional MRI (fMRI). In this imaging modality, an external sensory stimulus is applied to the subject, and MRI intensity changes are observed in brain regions in proximity to activated neurons. Several early papers by Ogawa et al. [139–141] used animal models to explore the image contrast mechanisms used in much of today's current fMRI methodologies. Shortly thereafter, these methods were successfully applied to humans [142,143]. Today, fMRI is the most widely used non-invasive method for investigating human brain response. Animal studies have played an important role in elucidating the physiological basis of the techniques that are used in humans. Also, they have provided basic insights into brain function; in this regard, fMRI is complementary to other more invasive methods, such as optical imaging and electrophysiology.

fMRI does not detect neuronal activation directly, but instead probes secondary hemodynamic changes; these include regional changes in cerebral blood volume (CBV), cerebral blood flow (CBF), and blood-oxygenation, which gives rise to the widely used blood-oxygen-level-dependent (BOLD) contrast mechanism [141]. BOLD contrast originates from regional perturbations in the magnetic susceptibility of brain tissue due to changes in the relative amounts of oxyhemoglobin to deoxyhemoglobin in the capillary bed, venules, and veins. These perturbations strongly affect the parameters T_2 and T_2^* in surrounding tissues because deoxyhemoglobin is paramagnetic, whereas oxyhemoglobin is diamagnetic

[144,145]. The relationship between changes in oxidative metabolism of activated neurons and the regional recruitment of excess blood oxyhemoglobin is an active area of investigation [146,147]. Several articles provide in-depth reviews of the current methods and understanding of the physiological basis of fMRI [146]. Pharmacological manipulation of the fMRI response in animals is not discussed here, and we refer the reader to a recent review on that topic [148].

An important experimental distinction between human fMRI studies, and the majority of animal studies, is that most of the animal work is performed on anesthetized subjects. Generally anesthesia is desirable to immobilize the animal and reduce motional image artifacts, as well as to minimize stress to the animal during the imaging session. However, its use may severely suppress the functional response in various brain regions due to their hypnotic and analgesic properties [149,150]. Furthermore, its use causes numerous physiological changes that may affect the fMRI response, such as alterations in cerebral blood pressure and respiratory depression. Thus, care must be taken when trying to ascertain the 'intrinsic' fMRI response of a subject, especially when making quantitative comparisons among different experiments. Different anesthesia types, or the same anesthesia at different doses, may cause variability in the results.

A commonly used anesthetic in fMRI rodents studies is α-chlorolose. This anesthetic does not significantly depress cortical activity [151] and provides a stable CBF [152]. However, α-chlorolose has numerous adverse side-effects, particularly the tendency to induce seizures. In order to avoid the adverse effects of anesthesia, several groups have investigated using mechanical restraining devices [153–155], or, in the case of primates, have trained the subject to remain still and visually fixate while in the magnet bore [156–158].

The BOLD effect was first studied in the rat brain by systemically modulating the inspired oxygen concentration or the anesthesia conditions [139–141]. It was noted that under hypoxic conditions fine vasculature within cortical gray matter was clearly identifiable and appeared hypointense. This effect was noted to be particularly evident in GE images and was attributed to T_2^* dephasing of water spins in proximity to vessels due to the presence of paramagnetic deoxyhemoglobin. These studies were conducted in rat using a 7 T imaging system. The BOLD contrast mechanism was later confirmed in cat using long TE-valued EPI at lower fields (2 T) [159]. The sensitivity to BOLD contrast is enhanced with increasing field strength, which is good news for the high field microscopist. Numerical simulations show the BOLD contribution to $1/T_2^*$ scales linearly with B_0 for large vessels (venules and veins) and quadratically for small vessels (capillaries) [59].

2.6. Metabolite imaging

Besides water protons and protons of lipids, there are many physiologically and biochemically important metabolites in the biological milieu that may be examined with μMR imaging techniques. Some of these are: *N*-acetyl aspartate (NAA), lactate, choline, creatine, *m*-inositol, and gamma-amino butyric acid (GABA). The presentation of images depicting the distribution of specific metabolites in the brain is of great interest in the study of normal and disease states and in the assessment of therapeutics. By extending the capability of μMRI to metabolite-specific imaging, a very useful and exciting area can be explored. However, the concentrations of most of the proton-bearing metabolites is, at best, in the millimolar range. Hence, the dominant water signal needs to be eliminated or suppressed and editing techniques need to be employed to differentiate the various metabolites. In addition the lipid signal, if present, needs to be suppressed as well. It is obvious that metabolite specific micro-imaging is a difficult challenge, especially in the face of reduced signal-to-noise and the need to deal with smaller voxel sizes. In this section, we briefly outline these challenges and assess the current status for carrying out metabolite-specific μMRI in small animals. In passing, we note that several of the important metabolites have received attention from the spectroscopic point of view but not from an imaging perspective. We will focus on lactate imaging since this metabolite has been studied extensively and serves well to illustrate the approaches available.

To reduce the field of view, it is often necessary to employ one of several single-voxel localization schemes such as PRESS, ISIS or STEAM [160].

With the incorporation of a chemical shift imaging (CSI) technique [161], one can obtain the spatial distribution of various metabolites. Water suppression is achieved using well-known pulse sequences [162,163], a commonly used one being CHESS [164]. Signals from coupled spins (e.g. lactate) can be separated from those of the uncoupled ones by suitable editing techniques. Towards this goal, polarization transfer, multiple quantum coherence transfer, spin-locking and different spectroscopic methods may be useful [165,166]. In a study of ischemic insult in the in vivo rat brain, the RF inhomogeneity produced by a surface coil was utilized to obtain a lactate map at a field of 4.7 T with a sequence composed of spin-locking pulses and a 2D spectroscopic imaging scheme [167]. This pulse sequence also ensured the suppression of lipid signals. However, the resulting voxel size was ~2 mm, which clearly highlights the difficulty of realizing microscopic imaging with this procedure.

Zero-quantum and multiple quantum based editing sequences combined with gradient selection of coherences have been shown to be powerful alternatives in metabolite imaging. A detailed discussion of pulse sequences suitable for MRI with proton-bearing metabolites has been given by Hurd and Freeman [168]. These authors discussed in particular the application of the gradient-based double quantum filter (DQF) method to lactate imaging [169,170]. deGraaf et al. [171] point out the necessity of working with larger voxel sizes because of signal loss arising from the incorporation of DQF coupled with the low lactate concentrations (<5 mM). He et al. [165] outlined a single-scan lactate editing method based on the selective homonuclear multiple quantum coherence-transfer (Sel-MQC) technique. Two types of pulse sequences were designed: one using a selective 180° pulse for CH_3 protons during the evolution period (SSel-MQC) and another using a hard 180° pulse for the CH_3 during the evolution period (HSel-MQC). Gradients were used to select the appropriate coherence pathways and provide suppression of the lipid signal. By extending the acquisition to a two scan sequence and using phase cycling, full recovery of the lactate intensity could be realized. A further advantage of the Sel-MQC sequence is its compatibility with CSI thus making it possible to obtain spatial maps of lactate distribution. Another pulse sequence, called SEE-SelMQC (spin-echo-enhanced SelMQC), has been described by He et al. [165]. It is used to suppress signals from tissues containing water and mobile lipids in a single scan and record ^1H resonances of multiple metabolites. Lactate images from murine EMT6 tumors obtained by He et al. [165] using MQC selection and CSI techniques achieved an in-plane resolution of 1.25 mm with a slice thickness of 6.6 mm. Choline images of the tumor were also studied, but with an in-plane resolution of only 1.6 mm and slice thickness of 9.6 mm. These studies were carried out at a field of 4.7 T.

Work of Kmiecik et al. [172] used a pulse sequence for lactate editing based on that of Trimble et al. [173] coupled with the 'spatial localization by imaging' (SLIM) method [174] and the generalized SLIM (GSLIM) method [175]. Both SLIM and GSLIM belong to a family of non-Fourier based signal processing methods and claim enhanced effective resolution by employing a priori information. The SLIM algorithm uses the high resolution water image to provide a priori spatial information. GSLIM is capable of yielding either spectra or metabolite maps like those from CSI. Kmiecik et al. [172] obtained 3D lactate imaging data from the muscle of the hind leg of a frog at sub-millimeter resolution in ~3 h. The high resolution images resulted from subsequent reconstruction with GSLIM. The effective resolution was quoted as $9.8 \times 9.8 \times 1300\ \mu m^3$. In view of the demonstrated improvement in resolution in proton spectra of cerebral metabolites at higher fields [176], a number of metabolites are likely candidates for μMRI. The CSI method can be integrated with the EPI method [177] to speed up image acquisitions. Guimaraes et al. [178] have obtained NAA images from the human brain in less than 13 min with a spatial resolution of 360 μl. The RARE method can also be integrated with CSI to reduce imaging time [179]. Further work in this direction is likely to contribute significantly to μMRI and neuroimaging of small animals.

Metabolites containing phosphorus such as phosphocreatine (PCr), ATP, and inorganic phosphate (Pi) are known to play important biochemical roles. Thus, it is of interest to explore the possibility of optimizing the voxel resolution in phosphorus (^{31}P) imaging. Although the natural abundance of ^{31}P is 100%, its sensitivity in relation to ^1H is only 6.6%.

The CSI method is, in principle, capable of yielding ^{31}P metabolite images, but there is a severe time penalty due to the low metabolite concentrations. Moreover in CSI, the localization of signals to specific voxels is compromised by chemical shift artifacts arising from misregistration and voxel bleeding [180–182]. Selective excitation can alleviate the problem to some extent. Loss in SNR due to intra-voxel dephasing of spins during the spatial-encoding in CSI, especially of short T_2 species, is also a problem [183]. Due to these limitations, voxel dimensions in ^{31}P metabolite images are generally of the order of a few millimeters. Using a smaller diameter coil, Skibbe et al. [184] were able to obtain Pi images at ~7 T from insect larva with an in-plane pixel dimension of 625×625 μm^2. With the use of higher fields and suitable post-processing procedures, it appears likely that ^{31}P metabolite imaging in small animals will soon reach the sub-millimeter domain.

2.7. More exotic imaging

2.7.1. Intermolecular zero and multiple quantum coherences

In spin-1/2 systems that are coupled by an intramolecular scalar interaction, it is possible to create zero and multiple quantum coherences that can be observed after converting them to single quantum coherences [185]. This principle has been extensively employed for imaging metabolites such as lactate. In systems where the spins are not coupled and the molecules are tumbling freely, one does not expect the possibility of creating these coherences between spins on different molecules. The dipolar interaction between molecules in an isotropic fluid averages out due to the tumbling motion. However, this averaging process is only effective on an NMR time scale over distances of the order of diffusion distance (i.e. a few microns). Dipolar averaging becomes less effective as the distance increases, and since a large number of spins are involved, the distant dipolar field (DDF) can survive at distances of order of 10–1000 μm.

Warren and co-workers [186–190] have pointed out that fairly simple pulse sequences can create intermolecular zero and multiple quantum coherences (i-ZQCs and i-MQCs) in liquids due to the DDF, and by converting them into single quantum coherences (SQCs), one can utilize them for imaging. The intensity of the higher order i-MQCs falls off rapidly, and from the imaging point of view, the i-ZQC and intermolecular double quantum coherence (i-DQC) signals are of interest. A typical i-ZQC/i-MQC pulse sequence starts with a 90° pulse followed by a gradient pulse of strength G and duration t that creates a magnetization helix of pitch $p = 2\pi/(\gamma G t)$. Coherences are created most effectively between spins that lie at a distance of $d = p/2$ [186,188]. A second RF pulse of appropriate flip angle is employed to convert the i-ZQCs/i-MQCs to SQCs. Gradient filtering and/or RF phase-cycling techniques [191] can be employed to filter out the desired coherences. The SQC signal is maximum when the gradient is along the B_0 axis (along the z-direction) and is half (sign reversed) in intensity with the gradient along x or y axis. The SQC signal disappears when the gradient axis is along the magic angle. These properties of the i-ZQCs and i-MQCs can be used to ensure the origin of these signals. The images obtained with i-ZQCs/i-MQCs are expected to exhibit unique contrast on account of their dependence on T_2 (ZQC) or T_2 (MQC) and the coherence distance d which can be altered to probe distances appropriate to the specimen under investigation. The duration between the first 90° pulse and the second reconversion RF pulse can be varied to provide contrast. The i-ZQC linewidth depends on the susceptibility variations in the region of the correlated spins, and this can also contribute to contrast. Furthermore, the i-ZQC and i-DQC signals exhibit proportionality to the square of the transverse magnetization, and thus they can provide good spin density contrast.

2.7.2. Dynamic displacement profile of water molecules: q-space imaging

The original PGSE method developed by Stejskal and Tanner [90] forms the basis of a technique called q-space imaging. In the PGSE sequence (90_x–g–180_y–g–echo), a pair of short duration gradient pulses, of width δ and strength g, is applied to the system separated by a period Δ. The resulting echo has a signal intensity $s(\vec{q})$ that depends on the dynamic displacement $\vec{R}$ of spins during the diffusion period $t = (\Delta - \delta/3)$. The signal intensity is measured with respect to that obtained without the application of the diffusion gradient. If the initial position of a spin is $\vec{r}_0$ and its position at the end of t is $\vec{r}$, then $\vec{r} - \vec{r}_0 = \vec{R}$.

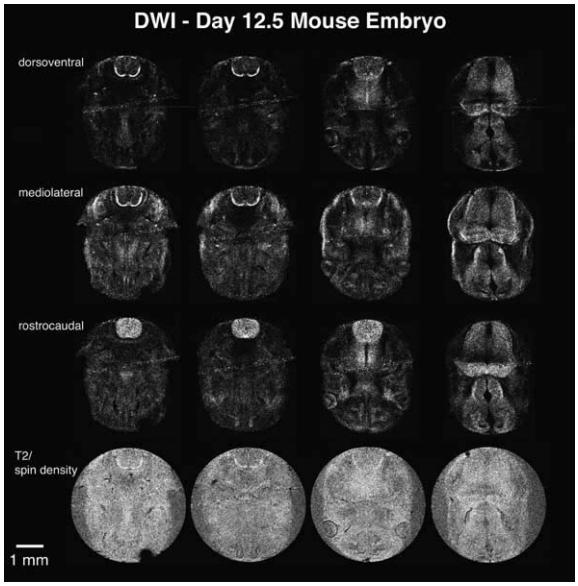

Fig. 4. DWIs of a fixed day 12.5 mouse embryo. The columns show four different slices with spinal cord evident in the top center of the left most three columns. In the top row, the diffusion gradient was applied in the dorsoventral direction (see arrow), mediolateral in the second row, rostrocaudal in the third row. The bottom row shows T_2/ spin density weighted images. Note the bright 'moustache' at the bottom of the spinal cord in the upper left four panels. This is the marginal zone that is not myelinated at this developmental stage, but the DWI images indicate that diffusion is clearly restricted in the dorsoventral and mediolateral directions, but not along the direction of the spinal cord (rostrocaudal).

The quantity $\vec{q}$ is defined as [47]:

$$\vec{q} = \left(\frac{1}{2\pi}\right)\gamma\vec{g}\delta. \tag{12}$$

It can be shown [47] that $s(\vec{q})$ bears a Fourier relationship to the quantity $P_s(\vec{r}_0|\vec{r}, t)$, the self-correlation function, which denotes the conditional probability that a spin initially at position $\vec{r}_0$ will undergo a displacement $\vec{R}$ over the diffusion period t.

$$s(\vec{q}) = \int \rho(\vec{r}_0)P_s(\vec{r}_0|r, t)\exp[\mathrm{i}2\pi\vec{q}(\vec{r} - \vec{r}_0)]\mathrm{d}\vec{r}\,\mathrm{d}\vec{r}_0, \tag{13}$$

where $\rho(r_0)$ is the spin density. Considering a displacement z along the gradient direction, the FT of $s(\vec{q})$ yields a displacement profile [192]

$$I(z) = \Im[s(\vec{q})] = \int \rho(\vec{r}_0)P_s(\vec{r}_0|(\vec{r}_0 + z), t)\mathrm{d}\vec{r}_0. \tag{14}$$

The FT relationship is precise only in the limit of 'narrow' diffusion gradient pulses.

The displacement profile is expressed as a convolution of $\rho(\vec{r}_0)$ and the conditional probability function, $P_s(\vec{r}_0|(\vec{r}_0 + z), t)$. With a fixed small value of δ, high q values are experimentally obtained using large gradients. The two gradient pulses in the PGSE method have to be well matched in area in order to avoid phase shifts. The pulse sequence PGSE-MASSEY proposed by Callaghan [193] is especially designed for compensating any mismatch in the two pulsed gradients. Instead of the spin-echo version, one can also use the stimulated echo version of PGSE (PGSTE) to carry out q-space imaging [192,194].

Thus, the usual form of the PGSE or PGSTE methods can yield both ADCs with lower gradient values and water displacement profiles at higher gradient strengths. A comparison of ADC distribution and displacement distribution may provide complementary insights in neuroimaging. The resolution in q-space imaging can far exceed the resolution in normal (k-space) imaging and is a unique probe of tissue microstructure. A displacement of a few μm can be measured with q-space imaging techniques.

3. Biological applications

3.1. Developmental biology

The study of embryonic and neonatal development in animal models is an application well suited to the multitude of capabilities offered by μMRI [102]. High resolution 3D imaging is needed to resolve fine details of the developing brain anatomy. Time-lapse μMRI allows one to visualize dynamical processes involved in brain development, such as morphological changes and patterns of cell migration. Quantitative imaging methods, such as DTI, provide information about developmental changes at the cellular and microstructure level. In this section, we review work in various embryonic and neonatal animal systems including mammalia, avians, and amphibia.

Visualizing axonal fiber connectivity in embryos has long been a goal of developmental neurobiologists. Conventional optical methods using stained histological sections, or by using fluorescent confocal microscopy, have numerous limitations for constructing

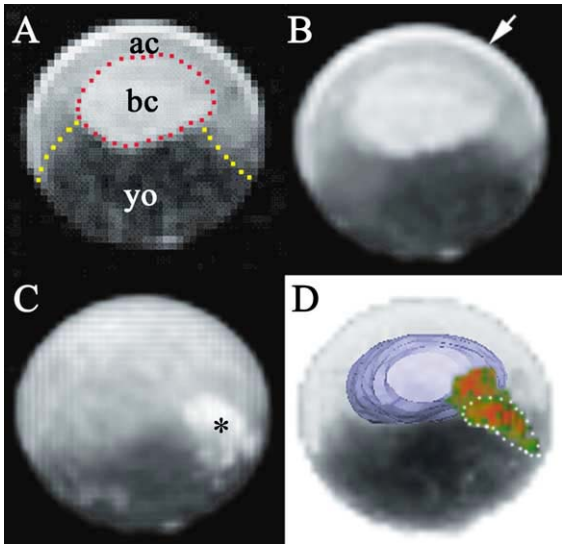

Fig. 5. In vivo 3D MR images of an early *X. laevis* embryo. One cell in the 32 cell embryo was injected with a gadolinium based contrast agent that stays within the labeled cell and all of its descendents. The embryo is in a dorso-dorso-lateral view with the dorso-ventral axis running from the front-right to the back-left. (A) A single slice is shown with the border between animal and vegetal drawn by yellow dots. ac: animal cap, bc: blastocoel, yo: yolk. (B) Half open volume, the arrow points to the liquid filled cleft between the vitelline membrane and the embryo. (C) Whole opaque volume, the labeled cells are marked with an asterisk. (D) Transparent volume with the blastocoel surface rendered by hand, the labeled clones detected using a 'seed fill' algorithm. The asterisk marks cells that can be seen on the outside of the embryo in (C). No color map has been applied to distinguish between the animal and the vegetal pole, so the difference between light and dark gray is purely endogenous contrast.

3D images of tracts in deep tissues [195]. Ahrens et al. [102] describe visualizations of premyelinated fiber pathways using DWI and DTI methods. The results clearly show premyelinated fibers in the marginal zone of the spinal cord in fixed day 12.5 mouse embryos at 20 μm resolution (see Fig. 4).

Novel methods for elucidating 3D microangiography in fixed mouse embryos have been described by Smith et al. [196,197]. These methods are effective in visualizing the entire vasculature (including neurovasculature) in embryos. In these studies, vasculature contrast is derived from gelatinous Gd-based contrast media that is perfused throughout the embryo via the umbilical vein.

Several groups report longitudinal studies of brain maturation in neonates [198–201]. In one of these studies [199], quantitative imaging was used to monitor changes in T_2 during the normal brain maturation process in dog and monkey. T_2 was observed to decrease with age for both white and gray matter. The decrease for white matter was more rapid compared to gray matter, presumably due to myelination. Diffusion weighted imaging (DWI) [200] has also been used to monitor brain myelination. In rat, it was shown that DWI is effective in detecting premyelinated fiber tracts in the neonatal brain before they become visible in T_1- or T_2-weighted images. More recent studies combined measurements of T_1, T_2, and the trace of the effective diffusion tensor to investigate brain maturation in kittens [201]. These results showed a high correlation between decreasing changes in trace-values and $1/T_2$ throughout the maturing brain; $1/T_1$-values exhibited a much lower correlation with the trace, but were more sensitive to the degree of myelination than was $1/T_2$.

Avian systems have been the subject of several in ovo studies [202–205]. Early studies were able to detect the cerebral ventricles, spinal cord, and other organs in a day 11 embryo [205]; Effmann et al. [204] made experimental refinements by exploring the use of RF surface coils and were able to study chick development at earlier stages (day 2–7) during the period of organogenisis.

Amphibians are a widely studied model system in vertebrate development and are ideal subjects for μMRI; the embryos have been studied extensively with both molecular biological and grafting approaches, are easily cultivated, undergo rapid development, and have large cells at early embryonic stages. Some of the very first microscopic magnetic resonance images produced [206] were of *Xenopus laevis* (African clawed frog) ova. These images, acquired at a resolution of $10 \times 13 \times 250\ \mu m^3$, resolved the cell nucleus and heterogeneity in the cytoplasm corresponding to animal and vegetal poles. The work of Jacobs and Fraser [207] used μMRI to follow cell lineages and cell movements over time in developing *Xenopus* embryos. For these lineage studies, a targeted cell from a 16-cell embryo was labeled intracellularly with Gd-DTPA-dextran agent via single-cell microinjection. The labeled embryo was allowed to develop in the magnet, while 3D volumetric images were acquired every

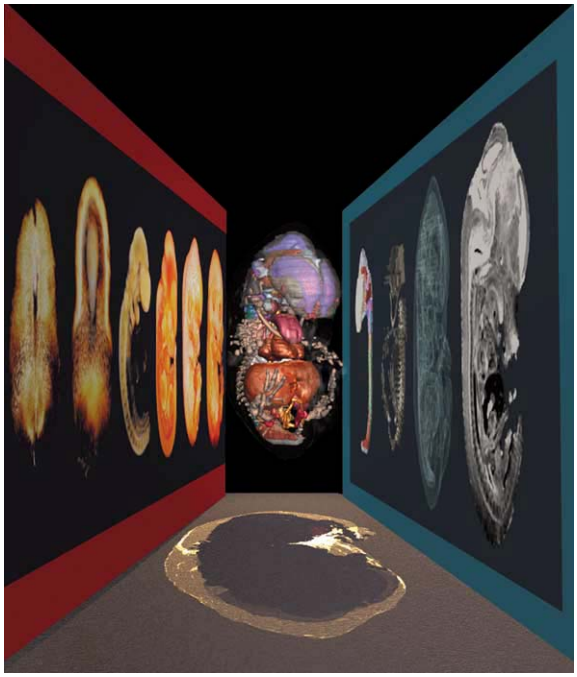

Fig. 6. Left and right panels show slices from 3D MR images of fixed mouse embryos at 8–14 days post-conception, the central 3D images is a model derived from the MRI data by outlining each anatomical structure, color coding each anatomical structure, smoothing, and surface rendering of the different structures. The image designed and created by Dr Seth Ruffins. For details, see the webpage http://mouseatlas.caltech.edu/.

few hours resulting in a time-lapse view of the labeled cells lineage and movements. Visualization of key events in the embryonic development, such as gastrulation and neurulation, was possible, as well as tracking the positions of both surface ectodermal and deep mesodermal cells [207]. Fig. 5 shows several renderings of an early gastrula stage *Xenopus* embryo where descendents of a single cell labeled several hours previous to the image acquisition are clearly visible.

Xenopus embryos and oocytes have also been used as test-bed for in vivo studies of intracellular MRI contrast agents that can be used for brain imaging [16,22,208,209]. Louie et al. [22] used μMRI of *Xenopus* tadpoles to demonstrate the effectiveness of a novel class of contrast agents that can visualize gene expression in vivo. Novel 'bifunctional' contrast agents [208] have also been tested in *Xenopus* that have the dual capability of being able to be detected with both conventional fluorescent microscopy and MRI.

3.2. Brain mapping

The construction of digital 3D anatomical atlases of CNS development using high resolution MRI is emerging as an important application. MRI provides a means of digitally recording anatomical information in three dimensions from intact specimens at reasonable spatial resolution. Although the rat, guinea pig, lemur, and oscine brain are reasonable candidates for atlas construction due to their relatively small size, the mouse is the prime candidate for such an atlas because of its importance in the study of many aspects of mammalian biology. Progress toward construction of a mouse embryo atlas from normal fixed specimens at various embryonic stages is described by several groups [102,196,210–213]. Fig. 6 shows representative images from one such atlas. The ultimate goal is to image a single (or small number) specimen over time and construct an in vivo atlas. Preliminary in utero images of mouse [214] and rat [215] embryos demonstrate the feasibility of non-invasively monitoring embryo development using μMRI. Phenotyping abnormal brain development is an extension of the μMRI-based atlas activities. In the studies of trisomy 16 mouse, a model system for human downs syndrome, μMRI has been used to investigate fixed day-17 embryos [216] exhibiting abnormal cerebellum development.

μMRI has also been shown to be effective in phenotyping abnormal embryonic brain development. Fragile-X knockout mice have been examined with MRI in an effort to compare various brain structures in these mice with those known to be abnormal in human fragile-X patients [217]. Although no size alterations were observed between the normal and knockout mice, this study demonstrated that quantifiable information about brain structures is straightforwardly obtained with MRI. In the studies of mouse models, μMRI has been used to compare and contrast normal and mutant embryos [216,218] exhibiting abnormal development. Although resolution is limited when compared to classical histological methods, the non-invasive nature of MRI makes it ideal for mouse phenotyping when longitudinal information is necessary.

Several studies of non-mouse systems indicate the general utility of μMRI in anatomical and functional studies of the brain. The guinea pig is an attractive

model system both for its size and robustness that allows extended in vivo experiments. T_2 values for gray and white matter have been determined for the in vivo guinea pig brain [219]. Using optimized hardware and imaging protocols, Gareau and co-workers were able to extract a fast (6 ms T_2) and a medium (48 ms T_2) relaxing component in white matter locations. Ohl et al. [220] have demonstrated that repeated reproducible in vivo measurements of hippocampal formation in the tree shrew are feasible with MRI. Although not a particular robust species, the avian is much studied in terms of development and learning [221]. Van der Linden and colleagues demonstrate that high resolution in vivo imaging of the canary is feasible. Their images reveal many large anatomical structures (e.g. ventricles) as well as a number of fiber tracts and subdivisions within the telencephalon. The common marmoset (*Callithrix jacchus*) is another model system tractable for in vivo MR studies [222,223]. As in all in vivo studies, the animal must remain stationary during the imaging, while being maintained in a safe and comfortable situation. Although gaseous isoflurane is an often used anesthetic in small animal work, an extensive marmoset MRI investigation revealed that continuous infusion of alphaxalone/alphadalone is a safe reliable alternative. The neonatal brain of the small primate mouse lemur (*Microcebus murinus*) was the subject of a rudimentary 3D μMRI atlas constructed by Ghosh et al. [224] using a 500 MHz imaging system. At 60 μm resolution many anatomical structures are clearly visible, including fine fiber tracts, laminations of cortices, details of the inner ear, and layering in the lateral geniculate nuclei.

3.3. Mn^{2+} tract tracing

Manganese is an essential trace element, but at high concentration can result in a syndrome of Parkinsonism and dystonia [225,226]. MRI has been useful in describing Mn effects in the brain [227,228]. Mn^{2+} is paramagnetic and has found significant use as an MRI contrast agent in chelated form [229,230]. Recently, Koretsky and co-workers have pioneered the use of the free Mn^{2+} ion as an activation dependent MRI agent to directly monitor brain function [231]. In essence, manganese is believed to mimic Ca^{2+}, acting as both an agonist and antagonist depending on concentration [232–235]. There is considerable in vivo evidence for the hypothesis that during neuronal activation Mn^{2+} can enter the cell through Ca^{2+} channels [236–238] and remains intracellular for extended periods of time [239–241]. Thus, Mn^{2+} will accumulate in neurons that have been active; causing a local shortening of water proton T_1, leading to a local increase in signal intensity in T_1-weighted MR images. Introduction of Mn^{2+} into brain parenchyma is the principle logistic problem in these experiments [242–247]. Thus far, most published reports have used venous infusion of $MnCl_2$ followed by a bolus of mannitol to break the blood-brain barrier (BBB), injection into the eye vitreous humor, or nasal application. Lin and Koretsky [231] showed that in unstimulated anesthetized rats this procedure afforded signal enhancement in ventricular regions of the brain due to accumulated Mn^{2+}. Rats undergoing Mn^{2+} infusion, mannitol BBB disruption, and stimulation on one side of the brain with glutamate displayed a large MRI signal increase in the cortex on the same side. Using a similar procedure, with the substitution of forepaw stimulation, Mn^{2+} activation specific signal enhancement was observed in the hemisphere contralateral to the stimulation. The very slow release of the ion after neuronal uptake affords the possibility of using Mn^{2+} accumulation to create a snapshot of neural activity in awake behaving animals that can then be assayed minutes or hours later using MRI. Lin and Koretsky [231] demonstrated this in an experiment where T_1-weighted brain images were recorded from an anesthetized rat that had previously been given Mn^{2+} while awake in a cage. They observed specific cortical activation. Along a similar line, Paulter et al. [248] showed that topical application of $MnCl_2$ solution to the naris of mice and intravitreal application to the retina leads to MRI signal enhancement along the respective neuronal pathways. Observations from this work lead to the interesting conclusion that Mn^{2+} can be passed from one neuron to the next along specific paths, presumably via synaptic junctions. Using a 9.4 T system, Kim and co-workers [249] have essentially repeated the forepaw stimulation experiments of Lin and Koretsky with the addition of simultaneous MRI BOLD and CBF measurements. Excellent spatial co-registration was observed among the Mn^{2+} associated synaptic activity, BOLD, and CBF activation maps. Although

the administration routes are somewhat cumbersome, the use of Mn^{2+} based methods to measure neuronal activation and trace specific functional tracts are compelling alternatives to fMRI and diffusion based MRI methods.

3.4. fMRI studies

3.4.1. Rodents

Numerous functional studies in rat primary somatosensory cortex have utilized the BOLD contrast mechanism. The first functional maps were reported by Hyder et al. [151] using an electrical stimulus to the forepaw. fMRI has been shown to be effective in identifying distinct forepaw and hindpaw cortical regions, consistent with results obtained from more invasive techniques [250]. Brinker et al. [251] investigated the feasibility of simultaneous monitoring of BOLD changes and evoked cortical potentials in response to forepaw stimulation and demonstrated a stimulus frequency-dependent response in both modalities. The BOLD contrast contributions from large vessels versus microvasculature in cortex at high magnetic field strength (9.4 T) was the subject of studies by Lee et al. [252]; using a forepaw stimulation assay, bipolar diffusion gradients were used to attenuate signal contributions from high mobility water protons in large vessels. It was observed that the gradients had less effect when used in the SE sequence, and it was argued that SE methods have a greater sensitivity to microvasculature in parenchyma compared to GE methods where large vessel contributions dominate. Another parameter recognized as affecting BOLD sensitivity is the inspired gas composition. In rats, studies by Hsu et al., show that mild hypocapnia significantly increases the size and magnitude of activation in peripheral somatosensory cortical regions observed by T_2^*-weighted imaging [253]. Inspired gas perturbations also have a significant impact on regional changes in CBV and CBF (discussed later).

In another rat somatosensory region, Yang et al. [254] mapped a single columnar whisker barrel in cortex. Later studies compared fMRI results in whisker barrel with the signatures obtained using electrophysiology [255]; it was shown that the activated areas had similar patterns and dimensions. The same group also demonstrated the ability of fMRI to detect odor-elicited activation in specific layers of the olfactory bulb [256]. Functional activation in the cerebellum in response to electrical stimulation has also been reported [257].

In addition to changes in blood-oxygenation, models of BOLD contrast include contributions from changes in CBV and CBF, and it is possible to experimentally isolate and study these latter two contributions. In fact, the first fMRI maps of human brain function utilized CBV contrast [258]. One method for detecting CBV changes is by using intravascular, high susceptibility, contrast agents, such as super-paramagnetic iron-oxide (SPIO) particles [259]. Using these agents, regional increases in blood volume in vasculature due to neuronal activation appear as a decrease in intensity in T_2 and T_2^*-weighted images. In rat, several studies have used this approach to investigate the CBV response to somatosensory stimulation. Mandeville et al. [260] used SPIO particles to examine the percent changes in CBV due to hypercarbia and also compared the fMRI signatures of blood-oxygenation magnetic susceptibility versus CBV changes during forepaw electrical stimulation. Kennan et al. [261] used a similar assay to model the relative intensity contributions from blood-oxygenation magnetic susceptibility effects and CBV.

CBF can be studied quantitatively using μMRI using various arterial spin-labeling methods [127,262,263]. The high magnetic field strengths used in μMRI is advantageous because, in addition to the increased sensitivity, the lengthening of T_1 provides a longer lifetime of the labeled spins. Changes in CBF have been used to detect the hemodynamic effects of neuronal activation in rat. Kerskens et al. [264] observed activation due to electrical stimulation in the forepaw using perfusion-weighted imaging and T_2^*-weighted BOLD images. Sensitivity to functional activation was more than ten times higher using the perfusion technique. Later, the same group showed that conditions of mild hypercapnia leads to significant up-regulation of the hemodynamic response and a large increase in the activation intensity in the perfusion-weighted images; the same conditions had much less impact on comparable BOLD images [265]. Using the same functional assay, Silva et al. [134] further examined the interplay between CBF increases and BOLD

signal changes. Simultaneous measurements of CBF and BOLD changes were recorded during the stimulus period. It was shown that the BOLD map was significantly larger than the CBF map, and the temporal response of the CBF increase was highly correlated with the BOLD signal changes [134]. The same investigators later showed that the onset of CBF changes in the cortex occurred approximately 0.5 s before BOLD changes were apparent [266]. It was also noted that the initial negative BOLD signal observed in other species (e.g. humans) [146] was absent in rat [266].

A handful of BOLD studies in rodents other than rat have been reported. In mouse, performing fMRI is significantly more challenging than in rat, and thus far, only limited results in this species have been reported. However, there are strong motives for investigating mouse due to the availability of numerous interesting genetically altered lines that have presumed alterations in neurofunction [48]. The mouse brain is significantly smaller in size than the rat brain. Consequently, extremely high SNR and resolution imaging capabilities are required. One group has reported BOLD signal changes in response to visual stimuli [267]. More recently, Ahrens and Dubowitz [48] have investigated extremely high resolution somatosensory fMRI in mice at 11.7 T using BOLD contrast. Using the gerbil model, Hess et al. [268] combined T_2^*-weighted imaging, optical recordings of intrinsic signals, and 2-deoxyglucose labeling methods to examine the hemodynamic basis of BOLD imaging in whisker barrel cortex. These data indicate that increased CBV and elevated deoxyhemoglobin contribute to the positive BOLD signal observed at the site of neuronal activation.

3.4.2. Non-rodent systems

Only a limited number of fMRI studies have been performed in animals larger than rodents, and this certainly will be an important future area of research. The cat is one example of a model system that has been used for studying the visual system. Much work has also been done in the macaque. However, primate work is beyond the scope of this review and we refer the reader to the original references [157,158]. The methodologies for performing BOLD contrast fMRI in cat were first described by Jezzard et al. [269]. These studies reported 0.7–2% signal changes in the primary visual cortex at 4.7 T using gaseous isoflurane anesthesia [269]. The cat has been used as a model system to study and map the columnar architecture of the visual cortex [270,271]. Kim et al. [270] have shown that activation maps generated at different time points along a biphasic BOLD response display varying degrees of neuronal localization; maps from the initial negative dip show greater neuronal localization compared to those from the latter positive BOLD response which show substantial venous recruitment. Using this observation, Kim et al. [270] report that it is possible to map visual iso-orientation columns from data acquired during the early initial dip in the BOLD response.

3.5. Autoimmune disease in the CNS

μMRI is a powerful tool in the study of autoimmune diseases of the CNS. Inappropriate immune responses to endogenous CNS antigens can have profoundly debilitating effects. This is the case for the common human disease, multiple sclerosis (MS). MS is a demyelinating disease that is characterized by the presence of both lymphocyte and macrophage infiltrates in perivascular regions of white matter. Demyelination can occur in almost any part of the CNS. This leads to a variety of visual and motor dysfunctions. MRI has long-served as an important tool for diagnosing and monitoring the progression of MS [272].

Progress in understanding MS has been assisted by the development of animal models. The most widely studied model for MS is experimental allergic encephalomyelitis (EAE). EAE is an inflammatory/demyelinating disease affecting the CNS. Many aspects of EAE pathology are similar to MS. EAE has been studied in numerous species (e.g. mouse, rat, guinea pig, monkeys). The disease is commonly induced by immunization with adjuvant mixed with CNS homogenates, purified myelin proteins, myelin-associated peptides, or by adoptive transfer of activated lymphocytes [273,274]. Also, transgenic mice have been engineered that spontaneously acquire the disease [275].

μMRI allows one to investigate the pathogenesis of the disease in a longitudinal fashion. This capability can be used to gain insights into the fundamental cellular and biochemical mechanisms of the disease, as well as to monitor the efficacy of therapeutics. A

number of imaging methods can be used to elucidate EAE lesions. Early studies [276–278] report increases in T_1 and T_2 in white matter regions containing EAE lesions, and these appear hypo- and hyper-intense in T_1- and T_2-weighted images, respectively. These observations are consistent with the presence of demyelination, inflammation, and edema. The use of intravenous contrast agents (e.g. Gd-DTPA) have been effective in elucidating active regions of breakdown in the BBB [279–284]. DWIs and ADC maps have been used to elucidate EAE lesions. Heide et al. [285] observed changes in DWIs on or before the day lesions became apparent in T_2-weighted images. In addition, anomalies in DWIs were observed that were not accompanied by T_2-weighted features. Verhoye et al. [286] report a significant correlation between increased ADCs and clinical score within white matter. Ahrens et al. [101] used DTI to assay the pathologic state of lesions in a transgenic EAE mouse model.

Cellular and molecular aspects of EAE have been investigated by several groups. Longitudinal studies have been used to test EAE inhibition treatments using antibodies against the intracellular adhesion molecule ICAM-1 [284], neurotrophic adrenocorticotrophic hormone analog peptides [287], and acylated myelin basic protein–peptide fragments [288]. In other studies, monocyte infiltration into the CNS, a common feature of EAE, was monitored in vivo using ^{19}F MRI of macrophages labeled with perfluoro-15-crown-5-ether [289]. Other experiments monitor the infiltration of inflammatory cells into the CNS using in situ labeling of macrophages with small superparamagnetic magnetite particles [290].

3.6. Neurodegeneration

Animal models of neurodegenerative diseases vary widely in their correspondence to the conditions in humans that they are claimed to model [291–294]. Model systems typically take the form of transgenic/knockout animals [295–297], drug-induced regimes [298–302], and fortuitous examples of mutations or 'normal' animals exhibiting symptoms or biochemical markers indicative of disease states [220,303,304]. The emerging importance of MRI in studying animal models of neurodegenerative disease is primarily due to its non-invasive nature enabling repeated measurements in long-term studies. Because this method provides information about tissue function within the context of anatomy and morphology will make it an invaluable adjunct to classic behavioral and histological methods.

The most basic use of MRI is the delineation of morphometric features. Where is a structure, what is its shape, how big is it, and how is it changing? Answering simple questions like these is of special importance in age-related neurodegenerative conditions (e.g. Alzheimer's disease (AD) and Parkinson's disease (PD)) and in assessing response to therapy. Although clinical MRI of AD and PD patients provides a wealth of information about anatomical correlates with these syndromes [305], MR studies of animal models and excised tissue are relatively uncommon. In the continuing hope that difference in T_1 and/or T_2 of plaques and tangles will provide contrast in MR images; Benveniste et al. [306] claim to be able to detect neuritic plaques in autopsy specimens form AD patients. It was necessary to use high resolution T_2^*-weighted imaging protocols at 9 T to distinguish plaques from the easily confused blood vessels. In a study of aging, Dhenain et al. [304,307] examined a small primate—the mouse lemur. They note considerable cerebral atrophy with age, also commonly observed in human AD. In an effort to mimic the pathology of AD, de la Torre [308,309] subjected young and aged rats to cerebrovascular insufficiency for extended times. They used ^{31}P and ^{1}H MRS and in vivo MRI to evaluate local CBF, local brain metabolite concentrations, and anatomy. They concluded that deficits (cognative, metabolic, and morphological) observed in this rat model mimic pathology reported in AD. Neuronal loss is a characteristic of both AD and PD in humans.

Lesions can be induced in rodent brains in a number of ways, principally via surgery or application of drugs (e.g. NMDA and 6-OHDA) and evaluated with μMRI techniques [310–312]. John et al. [313] used stereotaxic microinjection of NMDA into rat striatum to induce localized neuronal destruction. With T_2-weighted imaging, hyperintense parenchyma were visible after 12 h and up to 3 days later. The lateral ventricle adjacent to the injection became enlarged and was also hyperintense for the 4-week study period following the injection of NMDA. Subsequent histological examination confirmed that

the region of hyperintensity corresponded to the region of neuronal destruction and that the ventricle was enlarged. It is suggested in this study that the observed hyperintensity is due to both decreased T_2 (cystic changes) and greater water content (edema). No changes were observed in the contralateral sham injected side of the brain. Nguyen et al. [314] performed a more extended study employing 6-OHDA. They also correlated their MRI findings with PET studies. PET was used to evaluate the uptake of radiolabeled dopamine transporter and D2 receptor ligands, while MRI was used to determine local changes in hemodynamic response, such as CBF. Although performed at low field strength, a recent time-course study of a rat model of Huntington's disease showed how MRI can be used to study striatal graft development [315]. In this study individual animals were followed for up to 99 days after transplantation. Graft size and ventricle size obtained from MR images were found to be highly correlated with measures obtained from subsequent histologically processed sections. In a shorter time-course study [316], 3-nitropropionic acid intoxicated rats were employed as a model for Huntington's disease. T_2 and diffusion weighted MRI gave structural information, while regional relative CBV provided a measure of function. Lesions and altered perfusion in the striatum, hippocampus, and corpus callosum, but not in the cortex were observed 3 and 4.5 h after 3-nitropropionic acid injection. In a study using fixed specimens, Lester et al. [317] used high resolution MR images to identify brain regions and localization of excitotoxin-induced lesions. Subsequent histology confirmed the extent and location of the massive lesion. These authors note that the 3D digital nature of the MR images makes it straightforward to visualize and identify lesions by examining digitally generated sections in any plane, as well as by viewing semi-transparent volume renderings from any orientation.

3.7. Stroke

Stroke is the leading cause of brain damage in adults. Neurons are destroyed following either disruption of the cerebral blood supply or hemorrhage in the brain. Small animal model systems have been used for many years to investigate the basic biological mechanisms of tissue damage following hypoxia and ischemia. MRI offers the potential of being able to observe the process while it is happening; to map out the etiology, morphology, and topology of damage; to assess the efficacy of potential therapeutic regimes; and to develop MRI hardware and software that are directly applicable to use in patients. We note that there have been several recent reviews on a number of different MRI topics related to stroke [106,318–322].

In small animal work, as well as in the clinic, the vast majority of MRI work takes the form of straightforward T_1-, T_2-weighted, and ^{1}H-density protocols both with and without the addition of vascular contrast agents. These conventional methods have proved particularly useful in characterizing the location and extent of infarcts that follow several hours after the initial insult. More recently, protocols providing information about water diffusion and perfusion, and spectroscopy measurements giving direct information about concentrations of particular metabolites are being used in an increasing variety of studies. These newer methods are being used extensively in the assessment of the time response of the brain to ischemic/hypoxic insult.

Several groups have performed DWI at relatively widely spaced time points in a rat model of focal cerebral ischemia [323–326]. In these studies, the middle cerebral artery (MCA) was either permanently or transiently occluded. In general, increased DWI signal indicates areas of ischemia or infarct, which was confirmed by subsequent histological examination. Progressive changes in the volume of the hyperintense areas indicate the potential for differentiating so-called 'penumbral' regions from actual infarct. Moreover, DWI changes were observed in the first hour after MCA occlusion, while changes in T_2-weighted images were generally only observed after 2–3 h. Van Dorsten [327] measured both diffusion and perfusion weighted images after MCA occlusion, noting changes in both types of image and significant trends toward secondary lesion growth within 24 h. Moreover, in the gerbil it has been observed that changes in T_2 images are directly proportional to the duration of bicarotid artery occlusion [328]. In contrast, Gadian and co-workers [130,329–331] measured changes in T_2 within the first few minutes of ischemia, which they attribute to a local increase in deoxyhemoglobin levels.

The application of fast imaging techniques coupled with diffusion weighting provides adequate temporal resolution to test basic hypotheses about the origin of transient changes in the ADC of water in focal cerebral ischemia. Johnson and co-workers [332] performed a detailed time-course study of stroke volume; Moseley [333,334] used a diffusion weighted EPI protocol to obtain a temporal resolution of 12–16 s. Dijkhuizen et al. [335] performed combined repetitive DWI, T_2-weighted, and susceptibility contrast enhanced imaging before, during, and up to 5 h after unilateral hypoxia/ischemia. These studies all indicated significant local changes in water ADC within 5 min post-occlusion. Similar time courses were observed in other model systems, such as the gerbil [331,336] and feline [337,338]. In transient occlusion studies, ADC values showed recovery toward normal after reperfusion, although ADC changes appeared to poorly reflect ultimate tissue recovery.

Localized ^{1}H MR spectroscopic imaging (SI) allows one to determine whether abnormal spectroscopic markers are associated with focal lesions and to assess correlations between DWI changes and metabolic changes. Signal due to lactate becomes visible in ^{1}H spectra after MCA occlusion indicating the onset of anaerobic glycolysis in both rat [339,340] and feline models [341]. Repeated occlusion/reperfusion in the feline study [341] showed that lactate levels return to normal during early reperfusion. Signals from NAA decrease during hypoxia [339,340,342,343]. In a study using 6 and 7-day-old infant rats, Malisza et al. [344] observed significant differences between the two age groups. The 6-day animals showed no alteration in NAA levels, rapid lactate recovery after hypoxia, and no long-term damage. The 7-day animals exhibited decreased NAA, slow ($>$1 h) lactate recovery, and subsequent infarct. In all these studies, there was strict overlap between areas of ADC changes and areas of metabolite level changes. In a qualitatively different type of SI study, Dijkhuizen et al. [345] observed the incorporation of ^{13}C from infused 1-^{13}C-glucose into lactate. In the rat model, incorporation of the label was only observed in border zone (penumbral) regions, but not in the ischemic core.

MRI contrast agents have been used to track CBV, CBF, and vascular transit time before, during, and following transient and permanent MCA occlusion. Roberts et al. [346] have performed contrast-enhanced EPI to map out cerebrovascular parameters following MCAO in the feline. Caramia et al. [347] have also performed a detailed study using the feline model, 30 min transient MCA occlusion, and intravenous injections of the contrast agent Gd-BOPTA/dimeglumine. As expected, during occlusion the major areas showing changes in CBV were associated with the MCA, although some areas showed decreases (central) and some increases (peripheral). CBF likewise decreased in the central area, but was unchanged in the periphery. On reperfusion, CBF increased in the entire region and remained elevated for approximately 45 min, while CBV remained elevated on the hyperemic rim for $>$2 h. In a similar study, Zaharchuk et al. [132] used a long-lived macromolecular agent—MPEG-PL-DyDTPA, permitting continuous flow and volume measurements during transient focal ischemia. The use of BOLD contrast and T_2 agents appears to be less promising [348,349]. Signal changes disappear rapidly after magnetite injection and MCA occlusion, while BOLD sequences provide no additional information [348].

The ability of MRI to repeatedly image the same subject makes it an especially valuable tool in evaluating therapeutic treatment regimes for stroke. Treatment of embolic stroke in the rat model has been studied with a number of different imaging technique, including DWI, T_2-weighted, perfusion-weighted imaging, and measurements of CBF. Busch and coworkers [350,351] and Jiang et al. [352,353] have examined the effects of recombinant tissue type-plasminogen activator (rt-PA). In general, treatment with rt-PA soon after induction of thromboembolic stroke results in significant reperfusion of affected brain regions with lesion size and number reductions. Nonetheless, complete recovery was never observed. Spontaneously hypertensive stroke-prone rats are a much-studied system in stroke research and the time course of several therapies have been examined with MRI: Enalapril [354], the endothelin receptor subtype-A antagonist A127722 [355], and the fibrinogen lowering agent Ancrod [356]. Although efficacy of the treatments varied, MRI provided detailed real-time information about response of the animal to the treatment and in one case [355] treatment protocol was dependent upon observing changes in T_2-weighted

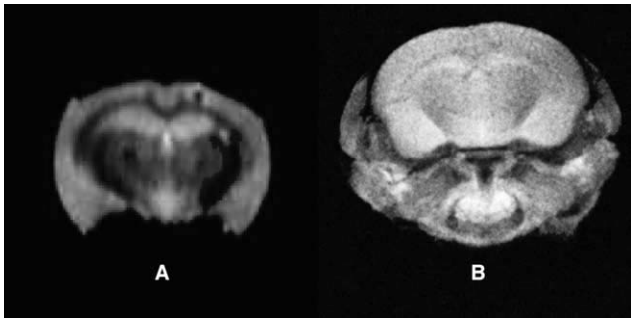

Fig. 7. The i-MQC images of a fixed mouse brain were obtained with a 11.7 T micro-imaging system. (A) shows the i-ZQC image of the mouse brain and (B) depicts the i-DQC image. The i-ZQC slice (390 μm thick) image was obtained with a FOV of 1.25×1.25 cm^2, Dim $= 128 \times 128$, TR $= 2$ *s* and coherence gradient $G_C = 5.6$ G. The 2D i-DQC image (slice thickness of 2 mm) was obtained with a FOV of 1.5×1.5 cm^2, TR $= 2$ s, dim $= 128 \times 128$, and coherence gradients in the ratio of 3.7:7.4 G.

MRI scans. Similarly, MRI has contributed to defining the effects of a number of 'neuro-protective' agents [353,357–360], as well as helping elucidate their mechanisms of action.

3.8. Trauma

Animal models for brain injury employ several methods to induce local and diffuse trauma, including controlled cortical impact (CCI), non-impact methods, and chemical insult. MRI has been used to examine morphological, structural, and biochemical changes concomitant to injury [361,362]. Using a cold-injury trauma rat brain model, Kamada et al. [363] applied both MRI and spectroscopy to show extensive development of edema and increased levels of lactate, acetate, and alanine, with dramatically decreased levels of NAA. The treatment of this model with 1,2-bis(nicotinamide)-propane (a free radical scavenger) showed significant decrease in edema and decrease in changes in levels of lactate, alanine, and NAA [364]. The determination of contusion volume using T_2-weighted MRI has been found to correlate satisfactorily with subsequent histological analysis [365], as did the location of pathological changes [366]. It should be noted that DWI and magnetization transfer (MT) techniques may be more accurate [367–369] methods to assess less drastic effects. In an evaluation of MT, Kimura et al. [370] found that mean magnetization transfer rates (MTR) in brain regions with axonal damage were significantly less than in regions without axonal damage. They observed these changes both in regions demonstrating high signal intensity images and in regions with no signal intensity change in T_2 weighted images. Forbes et al. [371] used arterial spin tagging to assess CBF and CO_2 reactivity in CCI by comparing populations with injury induced under normocarbia and hypocarbia. They found that hypocarbia narrowed the CBF distribution in the injured cortex. In an investigation of the time course of morphological changes in a rat fluid percussive injury model, MR images were recorded 2 and 90 days after injury. Hemorrhage, contusion, and brain edema were detected on day 2, while enlarged ventricles and cisterns were observed on day 90. Cecil et al. [372] performed a time-course study using both MRI and ^{1}H MRS with a pig diffuse injury model system. They observed that NAA/creatine was diminished by at least 20% in regions of confirmed axonal pathology, whereas their conventional MRI experiment detected no abnormalities. However using ^{31}P MRS at 1 h and 3 and 7 days post-injury, they found that widespread axonal injury was produced in the absence of changes in pH, PCr/Pi, or the concentrations of ATP [373].

3.9. More exotic imaging

3.9.1. i-ZQC and i-MQC brain imaging

i-ZQC images of a rat brain at 9.4 T have been obtained by Warren et al. [187]. These images, although comparable to the standard SE image, differ in their contrast. In the tumor region, the measured T_2 (ZQC) values are almost half of the T_2 (SQC) values. Kennedy et al. [374] have obtained i-DQC images of mouse tumors at 9.4 T and again the contrast exhibited

by the i-DQC images is different from those seen in T_1-weighted images but closer to those in T_2-weighted images. Narasimhan et al. [375] have obtained 3D MR microscopy i-ZQC and i-DQC images of a fixed mouse brain using different coherence length values. The d values (see Section 2.7.1) used by them correspond to the slice thickness along the field (z) direction. Although the images obtained were of very good quality, the variation with the helix pitch was not dramatic. This can be understood in terms of the role of diffusion and the effect of local gradients on the integrity of the magnetization helix especially its pitch and orientation in heterogeneous systems. Fig. 7 illustrates the quality of the images that can be generated with current technology. These images of a fixed mouse brain were obtained following procedures similar to those outlined by Narasimhan et al. [375]. Due to the lower SNR, the imaging time with i-ZQCs and i-MQCs is longer in comparison to standard imaging modalities. The possibility of 'tuning' contrast in these images using gradients is certainly unique. Further work may result in a reduction of imaging time and thus make imaging with these coherences attractive.

3.9.2. q-Space studies

In the context of small animal neuroimaging, q-space imaging of the mouse brain has been carried out by King and co-workers [376,377]. These authors examined the relationship between contrast in diffusion-weighted imaging and tissue morphology. Two groups of mice were studied—a normal group and another in which the blood supply to the forebrain was impaired surgically. An earlier study by these authors [376] did not employ localization techniques, while a later study [377] used a surface coil arrangement that resulted in better localization to an area in the brain. Displacement profiles of water protons were obtained and particular attention was paid to those protons with a probable displacement of ± 10 μm during the experimental diffusion period of 50 ms. The surgically treated group showed a larger proportion of water molecules undergoing such displacement in comparison to the normal group. In this regard, the ischemic and post-mortem results appear to be similar. Assaf et al. [378] have employed the q-space imaging approach to analyze diffusion-weighted images of excised spinal cord of stroke prone spontaneously hypertensive rats using large b values, where $b = \gamma^2 g^2 \delta^2 (\Delta - (\delta/3))$. Following the Cory–Garroway [192] procedure, these authors obtained the mean displacement and the probability for zero displacement from the water displacement profiles. Such a q-space analysis of the data enables one to distinguish clearly the normal from the demyelinated spinal cords of stroke prone spontaneously hypertensive rats. In another study, Assaf and Cohen [379] carried out the q-space analysis of water displacement probabilities from diffusion experimental data on rat brain (in vitro) using high b values.

These results on dynamic displacement of water molecules in mouse and rat brain and rat spinal cord provide structural information on the micron scale. These studies have an obvious bearing on stroke. With the availability of powerful gradient systems combined with the sensitivity advantage of high field MRI, one can expect q-space imaging to become a valuable adjunct to conventional k-space imaging.

4. Conclusions

The notion that microscopic resolution MRI might be feasible, and would certainly be exciting, was first proposed by Lauterbur in his initial description of the phenomenon in 1973 [380]. Since then the spatial resolution, quality, and applicability of μMRI have all increased dramatically. It is now straightforward to obtain 50 μm resolution in vivo 3D images of small animals in reasonable amounts of time. There is a vast array of microimaging protocols with new developments taking advantage of progress in both spin physics and clinical imaging realms. The recent surge in transgenic and mutant mouse model systems has emphasized the need for longitudinal in vivo imaging of opaque specimens in order to carry out phenotypic evaluations of these often rare and expensive animals. Although pushing the practical resolution beyond tens-of-microns is unlikely in the near future, much current research is aimed at improving temporal resolution, SNR, and CNR in μMRI. Advances in these areas coupled with the use of new contrast agents should bring this once esoteric methodology into the imaging mainstream.

Acknowledgements

REJ and PTN acknowledge support from the Human Brain Project with contributions from the National Institute on Drug Abuse and the National Institute of Mental Health (P20-DA08944), the National Center for Research Resources (R01-RR13625), the National Institute of Mental Health (MH61223), and the National Institute on Drug Abuse (R01-DA14930). ETA received support from the National Multiple Sclerosis Society (RG 3071A1/1), the National Eye Institute of the US National Institutes of Health (RO1 EY11933), and the National Science Foundation (CCR-0086065). TN and REJ gratefully acknowledge support from the Ministry of Education, Culture, Sports, Science, and Technology (Japan).

References

[1] P. Mansfield, P.G. Morris, NMR Imaging in Biomedicine, Academic Press, New York, 1982.
[2] P.T. Callaghan, Principles of Nuclear Magnetic Resonance Microscopy, Oxford University Press, New York, 1991.
[3] E.M. Haacke, R.W. Brown, M.R. Thompson, R. Venkatesan, Magnetic Resonance Imaging: Physical Principles and Sequence Design, Wiley, New York, 1999.
[4] F.W. Wehrli, Fast-Scan Magnetic Resonance: Principles and Applications, Raven Press, New York, 1990.
[5] M.L. Wood, in: D.D. Stark, W.G. Bradley Jr. (Eds.), Magnetic Resonance Imaging, vol. 1, Mosby, New York, 1992 chapter 2.
[6] W.A. Edelstein, J.M.S. Hutchison, G. Johnson, T. Redpath, Phys. Med. Biol. 25 (1980) 751.
[7] M.K. Stehling, R. Turner, P. Mansfield, Science 254 (1991) 43.
[8] A. Haase, J. Frahm, D. Matthaei, J. Magn. Reson. 67 (1986) 258.
[9] F. Schmitt, M.K. Stehling, R. Turner, Echo-Planar Imaging: Theory Technique, and Applications, Springer, New York, 1998.
[10] R.L. Ehman, J.P. Felmlee, Radiology 173 (1989) 255.
[11] R.E. Hendrick, U. Raff, in: D.D. Stark, W.G. Bradley (Eds.), Magnetic Resonance Imaging, vol. 1, Mosby, St. Louis, 1992, p. 109.
[12] E.M. Haacke, Magn. Reson. Med. 4 (1987) 407.
[13] J. Link, J. Seelig, J. Magn. Reson. 89 (1990) 310.
[14] S. Vinitski, R. Griffey, M. Fuka, N. Matwiyoff, R. Prost, Magn. Reson. Med. 5 (1987) 278.
[15] A.D. Watson, S.M. Rocklage, M.J. Carvlin, in: D.D. Stark, W.G. Bradley (Eds.), Magnetic Resonance Imaging, vol. 1, Mosby, St. Louis, 1992, p. 372.
[16] E.T. Ahrens, U. Rothbacher, R.E. Jacobs, S.E. Fraser, Proc. Natl Acad. Sci. USA 95 (1998) 8443.
[17] R. Weissleder, G. Elizondo, J. Wittenberg, C.A. Rabito, H.H. Bengele, L. Josephson, Radiology 175 (1990) 489.
[18] P. Gillis, S.H. Koenig, Magn. Reson. Med. 5 (1987) 323.
[19] R. Weissleder, Magn. Reson. Med. 22 (1991) 209.
[20] J.F. Kayyem, R.M. Kumar, S.E. Fraser, T.J. Meade, Chem. Biol. 2 (1995) 615.
[21] D. Hogemann, L. Josephson, R. Weissleder, J.P. Basilion, Bioconjugate Chem. 11 (2000) 941.
[22] A.Y. Louie, M.M. Huber, E.T. Ahrens, U. Rothbacher, R. Moats, R.E. Jacobs, S.E. Fraser, T.J. Meade, Nat. Biotechnol. 18 (2000) 321.
[23] W.H. Li, S.E. Fraser, T.J. Meade, J. Am. Chem. Soc. 121 (1999) 1413.
[24] R.E. Jacobs, E.T. Ahrens, T.J. Meade, S.E. Fraser, Trends Cell Biol. 9 (1999) 73.
[25] R. Weissleder, U. Mahmood, Radiology 219 (2001) 316.
[26] T. Meade, Acad. Radiol. 8 (2001) 1.
[27] C. Lok, Nature 412 (2001) 372.
[28] H.D.W. Hill, R.E. Richards, J. Phys. E 1 (1968) 977.
[29] D.I. Hoult, R.E. Richards, J. Magn. Reson. 24 (1976) 71.
[30] A. Abragam, The Principles of Nuclear Magnetism, Oxford University Press, Oxford, 1973.
[31] P.A. Bottomley, E.R. Andrew, Phys. Med. Biol. 23 (1978) 630.
[32] D.I. Hoult, P.C. Lauterbur, J. Magn. Reson. 34 (1979) 425.
[33] W.A. Edelstein, G.H. Glover, C.J. Hardy, R.W. Redington, Magn. Reson. Med. 3 (1986) 604.
[34] Z.H. Cho, C.B. Ahn, S.C. Juh, J.M. Jo, R.M. Friedenberg, S.E. Fraser, R.E. Jacobs, Philos. Trans. R. Soc. Lond. Ser. A—Math. Phys. Engng Sci. 333 (1990) 469.
[35] T.L. Peck, R.L. Magin, P.C. Lauterbur, J. Magn. Reson. Ser. B 108 (1995) 114.
[36] A.G. Webb, S.C. Grant, J. Magn. Reson. B 113 (1996) 83.
[37] P.M. Glover, R.W. Bowtell, G.D. Brown, P. Mansfield, Magn. Reson. Med. 31 (1994) 423.
[38] J.S. Schoeniger, S.J. Blackband, J. Magn. Reson. Ser. B 104 (1994) 127.
[39] P. Styles, N.F. Soffe, C.A. Scott, D.A. Cragg, F. Row, D.J. White, P.C.J. White, J. Magn. Reson. 60 (1984) 397.
[40] P. Styles, N.F. Soffe, C.A. Scott, J. Magn. Reson. 84 (1989) 376.
[41] E.W. McFarland, A. Mortara, Magn. Reson. Imaging 10 (1992) 279.
[42] A.C. Wright, H.K. Song, F.W. Wehrli, Magn. Reson. Med. 43 (2000) 163.
[43] R.D. Black, T.A. Early, P.B. Roemer, O.M. Mueller, A. Mogro-Campero, L.G. Turner, G.A. Johnson, Science 259 (1993) 793.
[44] F. Odoj, E. Rommel, M. von Kienlin, A. Haase, Rev. Sci. Instrum. 69 (1998) 2708.
[45] J.R. Miller, S.E. Hurlston, Q.Y. Ma, D.W. Face, D.J. Kountz, J.R. MacFall, L.W. Hedlund, G.A. Johnson, Magn. Reson. Med. 41 (1999) 72.
[46] P. Brunner, R.R. Ernst, J. Magn. Reson. 33 (1979) 83.
[47] P.T. Callaghan, Principles of Magnetic Resonance Microscopy, Oxford University Press, New York, 1991.
[48] E.T. Ahrens, D.J. Dubowitz, NMR Biomed. 14 (2001) 318.

[49] M.L. Wood, M.J. Bronskill, R.V. Mulkern, G.E. Santyr, J. Magn. Reson. Imaging 3 (S) (1993) 19.
[50] J. Frahm, K.D. Merboldt, W. Hanicke, Magn. Reson. Med. 6 (1988) 474.
[51] P.T. Callaghan, J. Magn. Reson. 87 (1990) 304.
[52] S. Posse, W.P. Aue, J. Magn. Reson. 88 (1990) 473.
[53] A.J. Lucas, S.J. Gibbs, E.W.G. Jones, M. Peyron, J.A. Derbyshire, L.D. Hall, J. Magn. Reson. Ser. A 104 (1993) 273.
[54] J.T. Mao, J.H. Gao, H. Yan, Magn. Reson. Med. 33 (1995) 582.
[55] R. Bhagwandien, R. Vanee, R. Beersma, C.J.G. Bakker, M.A. Moerland, J.J.W. Lagendijk, Magn. Reson. Imaging 10 (1992) 299.
[56] C.J.G. Bakker, R. Bhagwandien, M.A. Moerland, M. Fuderer, Magn. Reson. Imaging 11 (1993) 539.
[57] R. Bhagwandien, M.A. Moerland, C.J.G. Bakker, R. Beersma, J.J.W. Lagendijk, Magn. Reson. Imaging 12 (1994) 101.
[58] J.C. Sharp, J.K. Saunders, J. Magn. Reson. Ser. B 108 (1995) 58.
[59] S. Ogawa, R.S. Menon, D.W. Tank, S.G. Kim, H. Merkle, J.M. Ellermann, K. Ugurbil, Biophys. J. 64 (1993) 803.
[60] D.A. Yablonskiy, E.M. Haacke, Magn. Reson. Med. 32 (1994) 749.
[61] V.G. Kiselev, S. Posse, Magn. Reson. Med. 41 (1999) 499.
[62] J. Frahm, K.D. Merboldt, W. Hanicke, J. Magn. Reson. Ser. B 109 (1995) 234.
[63] J. Frahm, K.D. Merboldt, W. Hanicke, J. Magn. Reson. Ser. B 103 (1994) 91.
[64] Q.X. Yang, B.J. Dardzinski, S.Z. Li, P.J. Eslinger, M.B. Smith, Magn. Reson. Med. 37 (1997) 331.
[65] R.J. Ordidge, J.M. Gorell, J.C. Deniau, R.A. Knight, J.A. Helpern, Magn. Res. Med. 32 (1994) 335.
[66] Q.X. Yang, G.D. Williams, R.J. Demeure, T.J. Mosher, M.B. Smith, Magn. Reson. Med. 39 (1998) 402.
[67] Q.X. Yang, M.B. Smith, R.W. Briggs, R.E. Rycyna, Magn. Reson. Med. 141 (1999) 1.
[68] Z.H. Cho, Y.M. Ro, Magn. Reson. Med. 23 (1992) 193.
[69] G. Glover, S. Lai, Proceedings of the Sixth ISMRM, Sydney, Australia, 1998, p. 298.
[70] Y.M. Ro, Z.H. Cho, Magn. Reson. Med. 33 (1995) 521.
[71] J. Weis, U. Gorke, R. Kimmich, Magn. Reson. Imaging 14 (1996) 1165.
[72] E.M. Haacke, J.A. Tkach, T.B. Parrish, Radiology 170 (1989) 457.
[73] J.R. Reichenbach, R. Venkatesan, D.A. Yablonskiy, M.R. Thompson, S. Lai, E.M. Haacke, J. Magn. Reson. Imaging 7 (1997) 266.
[74] P.T. Callaghan, L.C. Forde, C.J. Rofe, J. Magn. Reson. B 104 (1994) 34.
[75] C.J. Rofe, J. Vannoort, P.J. Back, P.T. Callaghan, J. Magn. Reson. Ser. B 108 (1995) 125.
[76] S. Meiboom, D. Gill, Rev. Sci. Instrum. 29 (1958) 688.
[77] J.C. Sharp, R.W. Bowtell, P. Mansfield, Magn. Reson. Med. 29 (1993) 407.
[78] R.W. Bowtell, A. Peters, J.C. Sharp, P. Mansfield, E.W. Hsu, N. Aiken, A. Horsman, S.J. Blackband, Magn. Reson. Med. 33 (1995) 790.
[79] S. Emid, J.H.N. Creyghton, Physica B and C 128 (1985) 81.
[80] Z.H. Cho, Y.M. Ro, Magn. Reson. Med. 32 (1994) 258.
[81] S. Gravina, D.G. Cory, J. Magn. Reson. Ser. B 104 (1994) 53.
[82] J.K. Kim, D.B. Plewes, R.M. Henkelman, Magn. Reson. Med. 33 (1995) 497.
[83] J. Hennig, A. Nauerth, H. Friedburg, Magn. Reson. Med. 3 (1986) 823.
[84] J. Hennig, H. Friedburg, D. Ott, Magn. Reson. Med. 5 (1987) 380.
[85] J. Hennig, J. Magn. Reson. 78 (1988) 397.
[86] H.Y. Carr, E.M. Purcell, Phys. Rev. 94 (1954) 630.
[87] X.H. Zhou, G.P. Cofer, S.A. Suddarth, G.A. Johnson, Magn. Reson. Med. 30 (1993) 60.
[88] J. Ma, F.W. Wehrli, H.K. Song, Magn. Reson. Med. 35 (1996) 903.
[89] D. Le Bihan, Magn. Reson. Q 7 (1991) 1.
[90] E.O. Stejskal, J.E. Tanner, J. Chem. Phys. 42 (1965) 288.
[91] M.R. Merrill, J. Magn. Reson. A 103 (1994) 223.
[92] A.W. Anderson, J. Zhong, O.A. Petroff, A. Szafer, B.R. Ransom, J.W. Prichard, J.C. Gore, Magn. Reson. Med. 35 (1996) 162.
[93] J. Mattiello, P.J. Basser, J. Magn. Reson. Ser. A 108 (1994) 141.
[94] M. Neeman, J.P. Freyer, L.O. Sillerud, J. Magn. Reson. 90 (1990) 303.
[95] E.O. Stejskal, J. Phys. Chem. 43 (1965) 3597.
[96] D. Le Bihan, Diffusion and Perfusion Magnetic Resonance Imaging, Raven Press, New York, 1995.
[97] P.J. Basser, J. Mattiello, D. Le Bihan, J. Magn. Reson. B 103 (1994) 247.
[98] J. Mattiello, P.J. Basser, D. Le Bihan, Magn. Reson. Med. 37 (1997) 292.
[99] P.J. Basser, NMR Biomed. 8 (1995) 333.
[100] P.J. Basser, C. Pierpaoli, J. Magn. Reson. Ser. B 111 (1996) 209.
[101] E.T. Ahrens, D.H. Laidlaw, C. Readhead, C.F. Brosnan, S.E. Fraser, R.E. Jacobs, Magn. Reson. Med. 40 (1998) 119.
[102] E.T. Ahrens, J. Blumenthal, R.E. Jacobs, J.N. Giedd, in: A.W. Toga, J.C. Mazziotta (Eds.), Brain Mapping: The Systems, Academic Press, San Diego, 2000, p. 561.
[103] S. Mori, R. Itoh, J. Zhang, W.E. Kaufmann, P.C. van Zijl, M. Solaiyappan, P. Yarowsky, Magn. Reson. Med. 46 (2001) 18.
[104] C. Pierpaoli, P.J. Basser, Magn. Reson. Med. 36 (1996) 893.
[105] A. Ulug, P. van Zijl, J. Magn. Reson. Imaging 9 (1999) 804.
[106] N.J. Beauchamp Jr., A.M. Ulug, T.J. Passe, P.C. van Zijl, Radiographics 18 (1998) 1269.
[107] S. Mori, P.C. van Zijl, Magn. Reson. Med. 33 (1995) 41.
[108] E.C. Wong, R.W. Cox, A.W. Song, Magn. Reson. Med. 34 (1995) 139.
[109] T.E. Conturo, R.C. McKinstry, E. Akbudak, B.H. Robinson, Magn. Reson. Med. 35 (1996) 399.
[110] P.J. Basser, C. Pierpaoli, Magn. Reson. Med. 39 (1998) 928.
[111] M.E. Bastin, P.A. Armitage, I. Marshall, Magn. Reson. Imaging 16 (1998) 773.
[112] P. Armitage, M. Bastin, Magn. Reson. Med. 44 (2000) 117.
[113] P.A. Armitage, M.E. Bastin, Magn. Reson. Med. 45 (2001) 1056.

[114] P.J. Basser, S. Pajevic, Magn. Reson. Med. 44 (2000) 41.
[115] M. Bastin, P. Armitage, Magn. Reson. Imaging 18 (2000) 681.
[116] S. Boujraf, R. Luypaert, M. Osteaux, J. Appl. Clin. Med. Phys. 2 (2001) 178.
[117] R. Xue, P. van Zijl, B. Crain, M. Solaiyappan, S. Mori, Magn. Reson. Med. 42 (1999) 1123.
[118] R. Xue, M. Sawada, S. Goto, P.D. Hurn, R.J. Traystman, P.C. van Zijl, S. Mori, Magn. Reson. Med. 46 (2001) 183.
[119] C. Delalande, J.A. de Zwart, H. Trillaud, N. Grenier, C.T. Moonen, Magn. Reson. Med. 41 (1999) 1000.
[120] R. Luypaert, S. Boujraf, S. Sourbron, M. Osteaus, Eur. J. Radiol. 38 (2001) 19.
[121] D.L. Thomas, M.F. Lythgoe, G.S. Pell, F. Calamante, R.J. Ordidge, Phys. Med. Biol. 45 (2000) R97.
[122] E.L. Barbier, L. Lamalle, M. Decorps, J. Magn. Reson. Imaging 13 (2001) 496.
[123] D.S. Williams, J.A. Detre, J.S. Leigh, A.P. Koretsky, Proc. Natl Acad. Sci. USA 89 (1992) 212.
[124] W.G. Zhang, D.S. Williams, J.A. Detre, A.P. Koretsky, Magn. Reson. Med. 25 (1992) 362.
[125] J.A. Detre, W.G. Zhang, D.A. Roberts, A.C. Silva, D.S. Williams, D.J. Grandis, A.P. Koretsky, J.S. Leigh, NMR Biomed. 7 (1994) 75.
[126] J.A. Detre, J.S. Leigh, D.S. Williams, A.P. Koretsky, Magn. Reson. Imaging 23 (1992) 37.
[127] J.A. Detre, W. Zhang, D.A. Roberts, A.C. Silva, D.S. Williams, D.J. Grandis, A.P. Koretsky, J.S. Leigh, NMR Biomed. 7 (1994) 75.
[128] E.L. Barbier, A.C. Silva, H.J. Kim, D.S. Williams, A.P. Koretsky, Magn. Reson. Med. 41 (1999) 299.
[129] M. Gunther, M. Bock, L.R. Schad, Magn. Reson. Med. 46 (2001) 974.
[130] G.S. Pell, D.L. Thomas, M.F. Lythgoe, F. Calamante, A.M. Howseman, D.G. Gadian, R.J. Ordidge, Magn. Reson. Med. 41 (1999) 829.
[131] E.C. Wong, W.M. Luh, T.T. Liu, Magn. Reson. Med. 44 (2000) 511.
[132] G. Zaharchuk, A.A. Bogdanov Jr., J.J. Marota, M. Shimizu-Sasamata, R.M. Weisskoff, K.K. Kwong, B.G. Jenkins, R. Weissleder, B.R. Rosen, Magn. Reson. Med. 40 (1998) 666.
[133] D.C. Alsop, J.A. Detre, Radiology 208 (1998) 410.
[134] A.C. Silva, S.P. Lee, G. Yang, C. Iadecola, S.G. Kim, J. Cereb. Blood Flow Metab. 19 (1999) 871.
[135] W. Zhang, J. Magn. Reson. B 107 (1995) 165.
[136] E.C. Wong, R.B. Buxton, L.R. Frank, Neuroimaging Clin. N. Am. 9 (1999) 333.
[137] E.C. Wong, R.B. Buxton, L.R. Frank, Magn. Reson. Med. 40 (1998) 348.
[138] R.B. Buxton, L.R. Frank, E.C. Wong, B. Siewert, S. Warach, R.R. Edelman, Magn. Reson. Med. 40 (1998) 383.
[139] S. Ogawa, T.M. Lee, Magn. Reson. Med. 16 (1990) 9.
[140] S. Ogawa, T.M. Lee, A.S. Nayak, P. Glynn, Magn. Reson. Med. 14 (1990) 68.
[141] S. Ogawa, T.M. Lee, A.R. Kay, D.W. Tank, Proc. Natl Acad. Sci. USA 87 (1990) 9868.
[142] S. Ogawa, D.W. Tank, R. Menon, J.M. Ellermann, S.G. Kim, H. Merkle, K. Ugurbil, Proc. Natl Acad. Sci. USA 89 (1992) 5951.
[143] K.K. Kwong, J.W. Belliveau, D.A. Chesler, I.E. Goldberg, R.M. Weiskoff, B.P. Poncelet, D.N. Kennedy, B.E. Hoppel, M.S. Cohen, R. Turner, H.M. Cheng, T.J. Brady, B.R. Rosen, Proc. Natl Acad. Sci. USA 89 (1992) 5675.
[144] L. Pauling, C.D. Coryell, Proc. Natl Acad. Sci. USA 22 (1936) 210.
[145] K.R. Thulborn, J.C. Waterton, P.M. Matthews, G.K. Radda, Biochim. Biophys. Acta 714 (1982) 265.
[146] S. Ogawa, R.S. Menon, S.G. Kim, K. Ugurbil, Annu. Rev. Biophys. Biomolec. Struct. 27 (1998) 447.
[147] R.D. Hoge, J. Atkinson, B. Gill, G.R. Crelier, S. Marrett, G.B. Pike, Magn. Reson. Med. 42 (1999) 849.
[148] R.A. Leslie, M.F. James, Trends Pharmacol. Sci. 21 (2000) 314.
[149] S.M. Hayton, A. Kriss, D.P.R. Muller, Lab. Anim. 33 (1999) 243.
[150] H. Guggenberger, N.K. Logothetis, Anesthesiology 93 (2000) A94.
[151] F. Hyder, K.L. Behar, M.A. Martin, A.M. Blamire, R.G. Shulman, J. Cereb. Blood Flow Metab. 14 (1994) 649.
[152] U. Lindauer, A. Villringer, U. Dirnagl, Am. J. Physiol. 264 (1993) H1223.
[153] K.M. Lahti, C.F. Ferris, F.H. Li, C.H. Sotak, J.A. King, Magn. Reson. Med. 41 (1999) 412.
[154] K.M. Lahti, C.F. Ferris, F. Li, C.H. Sotak, J.A. King, J. Neurosci. Meth. 82 (1998) 75.
[155] A.M. Wyrwicz, N.K. Chen, L.M. Li, C. Weiss, J.F. Disterhoft, Magn. Reson. Med. 44 (2000) 474.
[156] N.K. Logothetis, H. Guggenberger, J. Pauls, Investig. Ophthalmol. Vis. Sci. 40 (1999) S818.
[157] N.K. Logothetis, H. Guggenberger, S. Peled, J. Pauls, Nat. Neurosci. 2 (1999) 555.
[158] N.K. Logothetis, Eur. J. Neurosci. 12 (2000) 183.
[159] R. Turner, B.D. Le, C.T.W. Moonen, D. Despres, J. Frank, Magn. Reson. Med. 22 (1991) 159.
[160] D.G. Gadian, NMR and Its Applications to Living Systems, Oxford University Press, New York, 1995.
[161] T.R. Brown, B.M. Kincaid, K. Ugurbil, Proc. Natl Acad. Sci. USA 79 (1982) 3523.
[162] P.J. Hore, Meth. Enzymol. 176 (1989) 64.
[163] P.C.M. van Zijl, C.T.W. Moonen, NMR Basic Principles and Progress, vol. 26, 1992, p. 67.
[164] A. Haase, J. Frahm, W. Haenicke, D. Matthei, Phys. Med. Biol. 30 (1985) 341.
[165] Q. He, D.L. Shungu, P.C.M. van Zijl, Z.M. Bhujwala, J.D. Glickson, J. Magn. Reson. B 106 (1995) 203.
[166] J. Star-Lack, D. Spielman, E. Adalsteinsson, J. Kurhanewicz, D.J. Terris, D.B. Vigneron, J. Magn. Reson. 133 (1998) 243.
[167] D. Bourgeois, P. Kozlowski, Magn. Reson. Med. 29 (1993) 402.
[168] R. Hurd, D.M. Freeman, Proc. Natl Acad. Sci. USA 86 (1989) 4402.
[169] R. Hurd, D.M. Freeman, NMR Biomed. 4 (1991) 73.
[170] D.M. Freeman, R. Hurd, NMR Basic Principles and Progress, vol. 27, 1992, p. 199.

[171] A.A. deGraaf, P.R. Luyten, J.A. den Hollander, W. Heindel, W.M.M.J. Bovee, Magn. Reson. Med. 30 (1993) 231.
[172] J.A. Kmiecik, C.D. Gregory, Z.P. Liang, D.E. Hrad, P.C. Lauterbur, M.J. Dawson, Magn. Reson. Med. 37 (1997) 840.
[173] L.A. Trimble, J.F. Shen, A.H. Wilman, P.S. Allen, J. Magn. Reson. 86 (1990) 191.
[174] X. Hu, D.N. Levin, P.C. Lauterbur, T.A. Spraggins, Magn. Reson. Med. 8 (1988) 314.
[175] Z.-P. Liang, P.C. Lauterbur, IEEE Trans. Med. Imaging 10 (1991) 132.
[176] R. Gruetter, S.A. Weisdorf, V. Rajanayagam, M. Terpstra, H. Merkle, C.L. Truwit, M. Garwood, S.L. Nyberg, K. Ugurbil, J. Magn. Reson. 135 (1998) 260.
[177] P. Mansfield, Magn. Reson. Med. 1 (1989) 370.
[178] A.R. Guimaraes, J.R. Baker, B.G. Jenkins, P.L. Lee, R.M. Weisskoff, B.R. Rosen, R.G. Gonzalez, Magn. Reson. Med. 41 (1999) 877.
[179] R. Mulkern, H. Chao, J. Bowers, D. Holtzman, Ann. NY Acad. Sci. 820 (1997) 97.
[180] Z. Wang, L. Bolinger, V.H. Subramanian, J.S. Leigh, J. Magn. Reson. 92 (1991) 64.
[181] T. Koch, G. Brix, W.J. Lorenz, J. Magn. Reson. B 104 (1994) 199.
[182] D.B. Twieg, H.P. Hetherington, S.L. Ponder, J. Den Hollander, G.M. Pohost, J. Magn. Reson. B 104 (1994) 153.
[183] A. Maudsley, J. Magn. Reson. 68 (1986) 363.
[184] U. Skibbe, J.T. Christeller, C.D. Eccles, W.A. Laing, P.T. Callaghan, J. Magn. Reson. Ser. B 108 (1995) 262.
[185] R.R. Ernst, G. Bodenhausen, A. Wokaun, Principles of Nuclear Magnetic Resonance in One and Two Dimensions, Clarendon Press, Oxford, 1992.
[186] W.S. Warren, W. Richter, A.H. Andreotti, B.T. Farmer, Science 262 (1993) 2005.
[187] W.S. Warren, S. Ahn, M. Mescher, M. Garwood, K. Ugurbil, W. Richter, R.R. Rizi, J. Hopkins, J.S. Leigh, Science 281 (1998) 247.
[188] W. Richter, S.H. Lee, W.S. Warren, Q.H. He, Science 267 (1995) 654.
[189] S. Lee, W. Richter, S. Vathyam, W.S. Warren, J. Chem. Phys. 105 (1996) 874.
[190] S. Vathyam, S. Lee, W.S. Warren, Science 272 (1996) 92.
[191] E.D. Minot, P.T. Callaghan, N. Kaplan, J. Magn. Reson. 140 (1999) 200.
[192] D.G. Cory, A.N. Garroway, Magn. Reson. Med. 14 (1990) 435.
[193] P.T. Callaghan, J. Magn. Reson. 88 (1990) 493.
[194] J.E. Tanner, J. Chem. Phys. 52 (1970) 2523.
[195] A.W. Toga, J.C. Mazziotta, Brain Mapping: The Methods, Academic Press, San Diego, 1996.
[196] B.R. Smith, G.A. Johnson, E.V. Groman, E. Linney, Proc. Natl Acad. Sci. USA 91 (1994) 3530.
[197] B.R. Smith, Sci. Am. 280 (1999) 76.
[198] E. Miot, D. Hoffschir, J.L. Poncy, R. Masse, A. Le Pape, S. Akoka, J. Med. Primatol. 24 (1995) 87.
[199] E. Miot-Noirault, L. Barantin, S. Akoka, A. Lepape, J. Neurosci. Meth. 72 (1997) 5.
[200] D.M. Wimberger, T.P. Roberts, A.J. Barkovich, L.M. Prayer, M.E. Moseley, J. Kucharczyk, J. Comput. Assist. Tomogr. 19 (1995) 28.
[201] C. Baratti, A.S. Barnett, C. Pierpaoli, Radiology 210 (1999) 133.
[202] A. Lirette, R.A. Towner, Z. Liu, E.G. Janzen, J.R. Chambers, R.W. Fairfull, L.P. Milligan, D.C. Crober, Poultry Sci. 72 (1993) 1411.
[203] B.R. Smith, E.L. Effmann, G.A. Johnson, J. Magn. Reson. Imaging 2 (1992) 237.
[204] E.L. Effmann, G.A. Johnson, B.R. Smith, G.A. Talbott, G. Cofer, Teratology 38 (1988) 59.
[205] S.N. Bone, G.A. Johnson, M.B. Thompson, Investig. Radiol. 21 (1986) 782.
[206] J.B. Aguayo, S.J. Blackband, J. Schoeniger, M.A. Mattingly, M. Hintermann, Nature (London) 322 (1986) 190.
[207] R.E. Jacobs, S.E. Fraser, Science 263 (1994) 681.
[208] M.M. Huber, A.B. Staubli, K. Kustedjo, M.H. Gray, J. Shih, S.E. Fraser, R.E. Jacobs, T.J. Meade, Bioconjugate Chem. 9 (1998) 242.
[209] S. Pauser, K. Keller, A. Zschunke, C. Mugge, Magn. Reson. Imaging 11 (1993) 419.
[210] B.R. Smith, E. Linney, D.S. Huff, G.A. Johnson, Comput. Med. Imaging Graph. 20 (1996) 483.
[211] B.R. Smith, D.S. Huff, G.A. Johnson, Comput. Med. Imaging Graph. 23 (1999) 33.
[212] R.E. Jacobs, E.T. Ahrens, M.E. Dickinson, D. Laidlaw, Comput. Med. Imaging Graph. 23 (1999) 15.
[213] M. Dhenain, S. Ruffins, R.E. Jacobs, Dev. Biol. 232 (2001) 458.
[214] P.T. Narasimhan, R.E. Jacobs, in: A.W. Toga, J.C. Mazziotta (Eds.), Brain Mapping: The Methods, Academic Press, New York, 1996, p. 147.
[215] B.R. Smith, M.D. Sattuck, L.W. Hedlund, G.A. Johnson, Magn. Reson. Med. 39 (1998) CP2.
[216] S. Kornguth, E. Bersu, M. Anderson, J. Markley, Teratology 45 (1992) 383.
[217] R.F. Kooy, E. Reyniers, M. Verhoye, J. Sijbers, C.E. Bakker, B.A. Oostra, P.J. Willems, A. Van der Linden, Eur. J. Hum. Genet. 7 (1999) 526.
[218] S. Kornguth, M. Anderson, J.L. Markley, A. Shedlovsky, Neuroimage 1 (1994) 220.
[219] P.J. Gareau, B.K. Rutt, C.V. Bowen, S.J. Karlik, J.R. Mitchell, Magn. Reson. Imaging 17 (1999) 1319.
[220] F. Ohl, T. Michaelis, H. Fujimori, J. Frahm, S. Rensing, E. Fuchs, J. Neurosci. Meth. 88 (1999) 189.
[221] A. Van der Linden, M. Verhoye, J. Van Audekerke, R. Peeters, M. Eens, S.W. Newman, T. Smulders, J. Balthazart, T.J. DeVoogd, J. Neurosci. Meth. 81 (1998) 45.
[222] V.M. Lee, N.G. Burdett, T.A. Carpenter, N.J. Herrod, M.F. James, L.D. Hall, ATLA—Altern. Lab. Anim. 26 (1998) 343.
[223] G. Whelan, M.F. James, N.A. Samson, N.I. Wood, Lab. Anim. 33 (1999) 24.
[224] P. Ghosh, M. O'Dell, P.T. Narasimhan, S.E. Fraser, R.E. Jacobs, Neuroimage 1 (1994) 345.
[225] Y.H. Kim, J.W. Kim, K.G. Ito, H.S. Lim, H.K. Cheong, J.Y. Kim, Y.C. Shin, K.S. Kim, Y.H. Moon, Neurotoxicology 20 (1999) 249.

[226] P.K. Pal, A. Samii, D.B. Calne, Neurotoxicology 20 (1999) 227.
[227] H. Eriksson, J. Tedroff, K.A. Thuomas, S.M. Aquilonius, P. Hartvig, K.J. Fasth, P. Bjurling, B. Langstrom, K.G. Hedstrom, E. Heilbronn, Arch. Toxicol. 66 (1992) 403.
[228] H. Shinotoh, B.J. Snow, K.A. Hewitt, B.D. Pate, D. Doudet, R. Nugent, D.P. Perl, W. Olanow, D.B. Calne, Neurology 45 (1995) 1199.
[229] C.F. Geraldes, A.D. Sherry, R.D. Brown, S.H. Koenig, Magn. Reson. Med. 3 (1986) 242.
[230] D. Fornasiero, J.C. Bellen, R.J. Baker, B.E. Chatterton, Investig. Radiol. 22 (1987) 322.
[231] Y.J. Lin, A.P. Koretsky, Magn. Reson. Med. 38 (1997) 378.
[232] P. Drapeau, D.A. Nachshen, J. Physiol.—Lond. 348 (1984) 493.
[233] K. Narita, F. Kawasaki, H. Kita, Brain Res. 510 (1990) 289.
[234] M. Aschner, J.L. Aschner, Neurosci. Biobehav. Rev. 15 (1991) 333.
[235] W. Low, N. Brawarnick, H. Rahaminoff, Biochem. Pharmacol. 42 (1991) 1537.
[236] H. Kita, K. Narita, W. Van Der Kloot, Brain Res. 205 (1981) 111.
[237] U. Meiti, R. Rahamimoff, Science 176 (1972) 308.
[238] T.J. Hallam, T.J. Rink, FEBS Lett. 186 (1985) 175.
[239] G.C. Cotzais, M.S. Horiuchi, S. Fuenzalida, I. Mena, Neurology 18 (1968).
[240] M.C. Newland, C. Cox, R. Hamada, G. Oberdoerster, B. Weiss, Fundam. Appl. Toxicol. 9 (1987).
[241] M.C. Newland, T.L. Ceckler, J.H. Kordower, B. Weiss, Exp. Neurol. 106 (1989) 251.
[242] M. Aschner, K.E. Vrana, W. Zheng, Neurotoxicology 20 (1999) 173.
[243] C. Calonder, P.I. Wurtenberger, R.P. Maguire, R. Pellikka, K.L. Leenders, J. Neurochem. 73 (1999) 2047.
[244] M. Aschner, Environ. Health Perspect. 108 (2000) 429.
[245] Y. Okuhata, Adv. Drug Delivery Rev. 37 (1999) 121.
[246] O. Rabin, L. Hegedus, J.M. Bourre, Q.R. Smith, J. Neurochem. 61 (1993) 509.
[247] N. Sotogaku, N. Oku, A. Takeda, J. Neurosci. Res. 61 (2000) 350.
[248] R.G. Pautler, A.C. Silva, A.P. Koretsky, Magn. Reson. Med. 40 (1998) 740.
[249] T.Q. Duong, A.C. Silva, S.P. Lee, S.G. Kim, Magn. Reson. Med. 43 (2000) 383.
[250] C. Bock, H. Krep, G. Brinker, M. Hoehn-Berlage, NMR Biomed. 11 (1998) 115.
[251] G. Brinker, C. Bock, E. Busch, H. Krep, K.A. Hossmann, M. Hoehn-Berlage, Magn. Reson. Med. 41 (1999) 469.
[252] S.P. Lee, A.C. Silva, K. Ugurbil, S.G. Kim, Magn. Reson. Med. 42 (1999) 919.
[253] E.W. Hsu, L.W. Hedlund, J.R. MacFall, Magn. Reson. Med. 40 (1998) 421.
[254] X.J. Yang, F. Hyder, R.G. Shulman, Proc. Natl Acad. Sci. USA 93 (1996) 475.
[255] X.J. Yang, F. Hyder, R.G. Shulman, Magn. Reson. Med. 38 (1997) 874.
[256] X.J. Yang, R. Renken, F. Hyder, M. Siddeek, C.A. Greer, G.M. Shepherd, R.G. Shulman, Proc. Natl Acad. Sci. USA 95 (1998) 7715.
[257] R.R. Peeters, M. Verhoye, B.P. Vos, D. Van Dyck, A. Van der Linden, E. De Schutter, Eur. J. Neurosci. 11 (1999) 2720.
[258] J.W. Belliveau, D.N. Kennedy, R.C. McKinstry, B.R. Buchbinder, R.M. Weisskoff, M.S. Cohen, J.M. Vevea, T.J. Brady, B.R. Rosen, Science 254 (1991) 716.
[259] R.P. Kennan, B.E. Scanley, J.C. Gore, Magn. Reson. Med. 37 (1997) 953.
[260] J.B. Mandeville, J.J. Marota, B.E. Kosofsky, J.R. Keltner, R. Weissleder, B.R. Rosen, R.M. Weisskoff, Magn. Reson. Med. 39 (1998) 615.
[261] R.P. Kennan, B.E. Scanley, R.B. Innis, J.C. Gore, Magn. Reson. Med. 40 (1998) 840.
[262] F. Calamante, D.L. Thomas, G.S. Pell, J. Wiersma, R. Turner, J. Cereb. Blood Flow Metab. 19 (1999) 701.
[263] D.S. Williams, J.A. Detre, J.S. Leigh, A.P. Koretsky, Proc. Natl Acad. Sci. USA 89 (1992) 212.
[264] C.M. Kerskens, M. Hoehn-Berlage, B. Schmitz, E. Busch, C. Bock, M.L. Gyngell, K.A. Hossmann, NMR Biomed. 9 (1996) 20.
[265] C. Bock, B. Schmitz, C.M. Kerskens, M.L. Gyngell, K.A. Hossmann, M. Hoehn-Berlage, Magn. Reson. Med. 39 (1998) 457.
[266] A.C. Silva, S.P. Lee, C. Iadecola, S.G. Kim, J. Cereb. Blood Flow Metab. 20 (2000) 201.
[267] W. Huang, I. Palyka, H.F. Li, E.M. Eisenstein, N.D. Volkow, C.S. Springer, Proc. Natl Acad. Sci. USA 93 (1996) 6037.
[268] A. Hess, D. Stiller, T. Kaulisch, P. Heil, H. Scheich, J. Neurosci. 20 (2000) 3328.
[269] P. Jezzard, J.P. Rauschecker, D. Malonek, Magn. Reson. Med. 38 (1997) 699.
[270] D.S. Kim, T.Q. Duong, S.G. Kim, Nat. Neurosci. 3 (2000) 164.
[271] T.Q. Duong, D.S. Kim, K. Ugurbil, S.G. Kim, Magn. Reson. Med. 44 (2000) 231.
[272] I.R. Young, A.S. Hall, C.A. Pallis, N.J. Legg, G.M. Bydder, R.E. Steiner, Lancet 2 (1981) 1063.
[273] C.S. Raine, Lab. Invest. 50 (1984) 608.
[274] R. Martin, H.F. McFarland, Crit. Rev. Clin. Lab. Sci. 32 (1995) 121.
[275] J. Goverman, A. Woods, L. Larson, L.P. Weiner, L. Hood, D.M. Zaller, Cell 72 (1993) 551.
[276] W.A. Steward, E.C. Alvord Jr., S. Hruby, L.D. Hall, D.W. Paty, Lancet 19 (1985).
[277] S.J. Karlik, J.J. Gilbert, C. Wong, M.K. Vandervoort, J.H. Noseworthy, Magn. Reson. Med. 14 (1990) 1.
[278] W.A. Stewart, E.C. Alvord, S. Hruby, L.D. Hall, D.W. Paty, Brain 114 (1991) 1069.
[279] C.P. Hawkins, P.M. Munro, F. MacKenzie, J. Kesselring, P.S. Tofts, E.P. du Boulay, D.N. Landon, W.I. McDonald, Brain 113 (1990) 365.
[280] C.P. Hawkins, F. Mackenzie, P. Tofts, E.P. du Boulay, W.I. McDonald, Brain 114 (1991) 801.
[281] I.J. Namer, J. Steibel, P. Poulet, J.P. Armspach, Y. Mauss, J. Chambron, Magn. Reson. Med. 24 (1992) 325.
[282] I.J. Namer, J. Steibel, P. Poulet, J.P. Armspach, M. Mohr, Y. Mauss, J. Chambron, Brain 116 (1993) 147.

[283] S.J. Karlik, E.A. Grant, D. Lee, J.H. Noseworthy, Magn. Reson. Med. 30 (1993) 326.
[284] S.P. Morrissey, R. Deichmann, J. Syha, C. Simonis, U. Zettl, J.J. Archelos, S. Jung, H. Stodal, H. Lassmann, K.V. Toyka, A. Haase, H.P. Hartung, J. Neuroimmunol. 69 (1996) 85.
[285] A.C. Heide, T.L. Richards, E.C. Alvord, J. Peterson, L.M. Rose, Magn. Reson. Med. 29 (1993) 478.
[286] M.R. Verhoye, E.J.'s- Gravenmade, E.R. Raman, J. Van Reempts, A. Van der Linden, Magn. Reson. Imaging 14 (1996) 521.
[287] H.J. Duckers, H.J. Muller, J. Verhaagen, K. Nicolay, W.H. Gispen, Neuroscience 77 (1997) 1163.
[288] S.J. Karlik, D. Munoz, J. St. Louis, G. Strejan, Magn. Reson. Imaging 17 (1999) 731.
[289] U. Noth, S.P. Morrissey, R. Deichmann, S. Jung, H. Adolf, A. Haase, J. Lutz, Artif. Cells Blood Substit. Immobil. Biotechnol. 25 (1997) 243.
[290] V. Dousset, C. Delalande, L. Ballarino, B. Quesson, D. Seilhan, M. Coussemacq, E. Thiaudiere, B. Brochet, P. Canioni, J.M. Caille, Magn. Reson. Med. 41 (1999) 329.
[291] M. Gallagher, Philos. Trans. R. Soc. Lond. Ser. B—Biol. Sci. 352 (1997) 1711.
[292] M. Goedert, M. Hasegawa, Am. J. Pathol. 154 (1999) 1.
[293] H. Mori, Neurobiol. Aging 19 (1998) S1.
[294] D.L. Price, G. Thinakaran, D.R. Borchelt, P.C.Y. Wong, M.K. Lee, L.J. Martin, S.S. Sisodia, J. Neurochem. 69 (1997) S256.
[295] C. Sturchler-Pierrat, B. Sommer, Rev. Neurosci. 10 (1999) 15.
[296] E. Masliah, Eur. J. Neurosci. 10 (1998) 111.
[297] M. Jucker, D.K. Ingram, Behav. Brain Res. 85 (1997) 1.
[298] M.B. Bogdanov, R.J. Ferrante, S. Kuemmerle, P. Klivenyi, M.F. Beal, J. Neurochem. 71 (1998) 2642.
[299] T.A. Jenkins, J.Y.F. Wong, D.W. Howells, F.A.O. Mendelsohn, S.Y. Chai, J. Neurochem. 73 (1999) 214.
[300] M. Mardiros, L. Butcher, J. Invest. Med. 46 (1998) 146A.
[301] G. Rozas, E. Lopez-Martin, M.J. Guerra, J.L. Labandeira-Garcia, J. Neurosci. Meth. 83 (1998) 165.
[302] K.N. Prasad, E.D. Clarkson, F.G. La Rosa, J. Edwards-Prasad, C.R. Freed, Mol. Genet. Metabol. 65 (1998) 1.
[303] F. Ohl, T. Michaelis, G.K. Vollmann-Honsdorf, C. Kirschbaum, E. Fuchs, Psychoneuroendocrinology 25 (2000) 357.
[304] M. Dhenain, A. Volk, J.L. Picq, M. Perret, F. Boller, J.L. Michot, Neurosci. Lett. 237 (1997) 85.
[305] R.J. Killiany, T. Gomez-Isla, M. Moss, R. Kikinis, T. Sandor, F. Jolesz, R. Tanzi, K. Jones, B.T. Hyman, M.S. Albert, Ann. Neurol. 47 (2000) 430.
[306] H. Benveniste, G. Einstein, K.R. Kim, C. Hulette, A. Johnson, Proc. Natl Acad. Sci. USA 96 (1999) 14079.
[307] M. Dhenain, C. Duyckaerts, J.L. Michot, A. Volk, J.L. Picq, F. Boller, Neurobiol. Aging 19 (1998) 65.
[308] J.C. de la Torre, T. Fortin, G.A. Park, K.S. Butler, P. Kozlowski, B.A. Pappas, H. de Socarraz, J.K. Saunders, M.T. Richard, Brain Res. 582 (1992) 186.
[309] J.C. de la Torre, K. Butler, P. Kozlowski, T. Fortin, J.K. Saunders, J. Neurosci. Res. 41 (1995) 238.
[310] P.R. Allegrini, D. Sauer, Magn. Reson. Imaging 10 (1992) 773.
[311] M. van Lookeren Campagne, J.B. Verheul, K. Nicolay, R. Balazs, J. Cereb. Blood Flow Metab. 14 (1994) 1011.
[312] R.M. Dijkhuizen, M. van Lookeren Campagne, T. Niendorf, W. Dreher, A. van der Toorn, M. Hoehn-Berlage, H.B. Verheul, C.A. Tulleken, D. Leibfritz, K.A. Hossmann, K. Nicolay, NMR Biomed. 9 (1996) 84.
[313] J. John, V. Govindaraju, P. Raghunathan, V.M. Kumar, Brain Res. Bull. 40 (1996) 273.
[314] T.V. Nguyen, A.L. Brownell, Y.C. Iris Chen, E. Livni, J.T. Coyle, B.R. Rosen, F. Cavagna, B.G. Jenkins, Synapse 36 (2000) 57.
[315] R. Guzman, M. Meyer, K.O. Lovblad, C. Ozdoba, G. Schroth, R.W. Seiler, H.R. Widmer, Exp. Neurol. 156 (1999) 180.
[316] T. Chyi, C. Chang, Neuroscience 92 (1999) 1035.
[317] D.S. Lester, R.C. Lyon, G.N. McGregor, R.T. Engelhardt, L.C. Schmued, G.A. Johnson, J.N. Johannessen, Neuroreport 10 (1999) 737.
[318] M. Rudin, N. Beckmann, R. Porszasz, T. Reese, D. Bochelen, A. Sauter, NMR Biomed. 12 (1999) 69.
[319] H.A. Rowley, P.E. Grant, T.P. Roberts, Neuroimaging Clin. N. Am. 9 (1999) 343.
[320] T.Q. Li, Z.G. Chen, T. Hindmarsh, Acta Radiol. 39 (1998) 460.
[321] A.E. Baird, S. Warach, J. Cereb. Blood Flow Metab. 18 (1998) 583.
[322] M. Rudin, N. Beckmann, A. Mir, A. Sauter, Eur. J. Pharm. Sci. 3 (1995) 255.
[323] R. Gill, N.R. Sibson, R.H. Hatfield, N.G. Burdett, T.A. Carpenter, L.D. Hall, J.D. Pickard, J. Cereb. Blood Flow Metab. 15 (1995) 1.
[324] A.D. Perez-Trepichio, M. Xue, T.C. Ng, A.W. Majors, A.J. Furlan, I.A. Awad, S.C. Jones, Stroke 26 (1995) 667.
[325] A.R. Pierce, E.H. Lo, J.B. Mandeville, R.G. Gonzalez, B.R. Rosen, G.L. Wolf, J. Cereb. Blood Flow Metab. 17 (1997) 183.
[326] M.F. Lythgoe, D.L. Thomas, F. Calamante, G.S. Pell, M.D. King, A.L. Busza, C.H. Sotak, S.R. Williams, R.J. Ordidge, D.G. Gadian, Magn. Reson. Med. 44 (2000) 706.
[327] F.A. van Dorsten, R. Hata, K. Maeda, C. Franke, M. Eis, K.A. Hossmann, M. Hoehn, NMR Biomed. 12 (1999) 525.
[328] T. Messager, F. Franconi, L. Lemaire, J.M. De Bray, J.P. Saint Andre, P. Jallet, J.J. Le Juene, Investig. Radiol. 35 (2000) 180.
[329] D.L. Thomas, G.S. Pell, M.F. Lythgoe, D.G. Gadian, R.J. Ordidge, Magn. Reson. Med. 39 (1998) 950.
[330] F. Calamante, M.F. Lythgoe, G.S. Pell, D.L. Thomas, M.D. King, A.L. Busza, C.H. Sotak, S.R. Williams, R.J. Ordidge, D.G. Gadian, Magn. Reson. Med. 41 (1999) 479.
[331] G.S. Pell, M.F. Lythgoe, D.L. Thomas, F. Calamante, M.D. King, D.G. Gadian, R.J. Ordidge, Stroke 30 (1999) 1263.
[332] W.L. Hall, H. Benveniste, L.W. Hedlund, G.A. Johnson, Neuroimage 3 (1996) 158.
[333] J. Rother, A.J. de Crespigny, H. D'Arceuil, M.E. Moseley, J. Cereb. Blood Flow Metab. 16 (1996) 214.
[334] J. Rother, A.J. de Crespigny, H. D'Arceuil, K. Iwai, M.E. Moseley, Stroke 27 (1996) 980.

[335] R.M. Dijkhuizen, S. Knollema, H.B. van der Worp, G.J. Ter Horst, D.J. De Wildt, J.W. Berkelbach van der Sprenkel, K.A. Tulleken, K. Nicolay, Stroke 29 (1998) 695.
[336] H. Lei, P. Dooley, J. Peeling, D. Corbett, Neurosci. Lett. 257 (1998) 105.
[337] C. Pierpaoli, J.R. Alger, A. Righini, J. Mattiello, R. Dickerson, D. Des Pres, A. Barnett, G. Di Chiro, J. Cereb. Blood Flow Metab. 16 (1996) 892.
[338] T. Kuroiwa, T. Nagaoka, M. Ueki, I. Yamada, N. Miyasaka, H. Akimoto, Stroke 29 (1998) 859.
[339] M.L. Gyngell, E. Busch, B. Schmitz, K. Kohno, T. Back, M. Hoehn-Berlage, K.A. Hossmann, NMR Biomed. 8 (1995) 206.
[340] D.G. Norris, M. Hoehn-Berlage, W. Dreher, K. Kohno, E. Busch, B. Schmitz, J. Cereb. Blood Flow Metab. 18 (1998) 749.
[341] A. Bizzi, A. Righini, R. Turner, D. Le Bihan, K.H. Bockhorst, J.R. Alger, Magn. Reson. Imaging 14 (1996) 581.
[342] W. Dreher, B. Kuhn, M.L. Gyngell, E. Busch, T. Niendorf, K.A. Hossmann, D. Leibfritz, Magn. Reson. Med. 39 (1998) 878.
[343] D. Hesselbarth, C. Franke, R. Hata, G. Brinker, M. Hoehn-Berlage, NMR Biomed. 11 (1998) 423.
[344] K.L. Malisza, P. Kozlowski, G. Ning, S. Bascaramurty, U.I. Tuor, NMR Biomed. 12 (1999) 31.
[345] R.M. Dijkhuizen, R.A. de Graaf, M. Garwood, K.A. Tulleken, K. Nicolay, J. Cereb. Blood Flow Metab. 19 (1999) 376.
[346] T.P.L. Roberts, Z.S. Vexler, V. Vexler, N. Derugin, J. Kucharczyk, Eur. Radiol. 6 (1996) 645.
[347] F. Caramia, Z. Huang, L.M. Hamberg, R.M. Weisskoff, G. Zaharchuk, M.A. Moskowitz, F.M. Cavagna, B.R. Rosen, Magn. Reson. Imaging 16 (1998) 97.
[348] R.A. Jones, T.B. Muller, O. Haraldseth, A.M. Baptista, A.N. Oksendal, Magn. Reson. Med. 35 (1996) 489.
[349] M. Hisakane, Y. Katayama, H. Igarashi, A. Terashi, Nippon Ika Daigaku Zasshi 65 (1998) 135.
[350] E. Busch, K. Kruger, K. Fritze, P.R. Allegrini, M. Hoehn-Berlage, K.A. Hossmann, Acta Neurochir Suppl. (Wien) 70 (1997) 206.
[351] E. Busch, K. Kruger, P.R. Allegrini, C.M. Kerskens, M.L. Gyngell, M. Hoehn-Berlage, K.A. Hossmann, J. Cereb. Blood Flow Metab. 18 (1998) 407.
[352] Q. Jiang, Z.G. Zhang, R.L. Zhang, J.R. Ewing, G.W. Divine, P. Jiang, M. Chopp, Brain Res. 788 (1998) 191.
[353] Q. Jiang, Z.G. Zhang, R.L. Zhang, J.R. Ewing, G.W. Divine, P. Jiang, M. Chopp, Fibrinolysis Proteolysis 12 (1998) 33.
[354] E.L. Blezer, K. Nicolay, D. Bar, R. Goldschmeding, G.H. Jansen, H.A. Koomans, J.A. Joles, Stroke 29 (1998) 1671.
[355] E.L. Blezer, K. Nicolay, R. Goldschmeding, G.H. Jansen, H.A. Koomans, T.J. Rabelink, J.A. Joles, Hypertension 33 (1999) 137.
[356] B. Elger, W. Hornberger, M. Schwarz, J. Seega, Eur. J. Pharmacol. 336 (1997) 7.
[357] L. Belayev, W. Zhao, P.M. Pattany, R.G. Weaver, P.W. Huh, B. Lin, R. Busto, M.D. Ginsberg, Stroke 29 (1998) 2587.
[358] B.C. Albensi, M.P. Schweizer, T.M. Rarick, F. Filloux, Investig. Radiol. 34 (1999) 249.
[359] D. Bochelen, M. Rudin, A. Sauter, J. Pharmacol. Exp. Ther. 288 (1999) 653.
[360] U.I. Tuor, K.L. Malisza, P. Kozlowski, Exp. Brain Res. 125 (1999) 217.
[361] K. Nicolay, R.M. Dijkhuizen, A. van der Toorn, T. Reese, D. Brandsma, M. de Boer, H.J. Muller, G. van Vliet, K.S. Tamminga, J.W.B. van der Sprenkel, H.B. Verheul, C.A.F. Tulleken, M. van Lookeren Campagne, B.M. Spruijt, Acta Neuropsychiatr. 8 (1996) 76.
[362] R. Duvdevani, A. Demitrochenko, N. Knoller, O. Mayzel, Y. Assaf, Y. Cohen, Neurosci. Lett. (1997) S15.
[363] K. Kamada, K. Houkin, K. Hida, Y. Iwasaki, H. Abe, Neurol. Med. Chir. (Tokyo) 35 (1995) 1.
[364] K. Kamada, Hokkaido Igaku Zasshi 71 (1996) 105.
[365] O.M. Kochanek, D.W. Marion, W.G. Zhang, J.K. Schiding, M. White, A.M. Palmer, R.S.B. Clark, M.E. Omalley, S.D. Styren, C. Ho, S.T. DeKosky, J. Neurotrauma 12 (1995) 1015.
[366] L. Qian, T. Nagaoka, K. Ohno, B. Tominaga, T. Nariai, K. Hirakawa, T. Kuroiwa, K. Takakuda, H. Miyairi, Bull. Tokyo Med. Dent. Univ. 43 (1996) 53.
[367] D.H. Smith, D.F. Meaney, R.E. Lenkinski, D.C. Alsop, R. Grossman, H. Kimura, T.K. McIntosh, T.A. Gennarelli, J. Neurotrauma 12 (1995) 573.
[368] D.C. Alsop, H. Murai, J.A. Detre, T.K. McIntosh, D.H. Smith, J. Neurotrauma 13 (1996) 515.
[369] J. Ito, A. Marmarou, P. Barzo, P. Fatouros, F. Corwin, J. Neurosurg. 84 (1996) 97.
[370] H. Kimura, D.F. Meaney, J.C. McGowan, R.I. Grossman, R.E. Lenkinski, D.T. Ross, T.K. McIntosh, T.A. Gennarelli, D.H. Smith, J. Comput. Assist. Tomogr. 20 (1996) 540.
[371] M.L. Forbes, K.S. Hendrich, P.M. Kochanek, D.S. Williams, J.K. Schiding, S.R. Wisniewski, S.F. Kelsey, S.T. DeKosky, S.H. Graham, D.W. Marion, C. Ho, J. Cereb. Blood Flow Metab. 17 (1997) 865.
[372] K.M. Cecil, R.E. Lenkinski, D.F. Meaney, T.K. McIntosh, D.H. Smith, J. Neurochem. 70 (1998) 2038.
[373] D.H. Smith, K.M. Cecil, D.F. Meaney, X.H. Chen, T.K. McIntosh, T.A. Gennarelli, R.E. Lenkinski, J. Neurotrauma 15 (1998) 665.
[374] S.D. Kennedy, Z. Chen, P. Connelly, J.H. Zhong, Proc. Int. Soc. Magn. Reson. Med. 8 (2000) 437.
[375] P.T. Narasimhan, S. Velan, R.E. Jacobs, Proc. Int. Soc. Magn. Reson. Med. 8 (2000) 2074.
[376] M.D. King, J. Houseman, S.A. Roussel, N. van Bruggen, S.R. Williams, D.G. Gadian, Magn. Reson. Med. 32 (1994) 707.
[377] M.D. King, J. Houseman, D.G. Gadian, A. Connelly, Magn. Reson. Med. 38 (1997) 930.
[378] Y. Assaf, A. Mayk, Y. Cohen, Proc. Int. Soc. Mag. Reson. Med. 8 (2000) 470.
[379] Y. Assaf, A. Mayk, Y. Cohen, Magn. Reson. Med. 44 (2000) 713.
[380] P.C. Lauterbur, Nature 242 (1973) 190.